Petroleum Science 23 (2026) 3408–3438

Contents lists available at ScienceDirect

Petroleum Science

journal homepage: www.keaipublishing.com/en/journals/petroleum-science

Original Paper

A facies-constrained flow-network model for fast history matching and production optimization of polymer flooding reservoirs

Guo-Yu Qin [a,b], Xia Yan [a,b,*], Kai Zhang [b,c], Li-Ming Zhang [a,b], Qi Zhang [d], Ming-Xin Zhang [a,b], Chen-Yang Wang [a,b]

[a] National Key Laboratory of Deep Oil and Gas, China University of Petroleum (East China), Qingdao, 266580, Shandong, China
[b] School of Petroleum Engineering, China University of Petroleum (East China), Qingdao, 266580, Shandong, China
[c] Civil Engineering School, Qingdao University of Technology, Qingdao, 266520, Shandong, China
[d] Department of Civil and Environmental Engineering, University of Macau, Taipa, 999078, Macao, China

A R T I C L E I N F O

Article history:
Received 17 March 2025
Received in revised form
20 December 2025
Accepted 3 February 2026
Available online 9 February 2026

Edited by Meng-Jiao Zhou

Keywords:
Physics-based data-driven model
Sedimentary facies constraints
Polymer flooding
History matching
Production optimization

A B S T R A C T

With the rising water cut in mature oil fields, polymer flooding has emerged as a critical Enhanced Oil Recovery (EOR) technique. However, high-fidelity numerical simulations for history matching and polymer flooding optimization remain computationally intensive, limiting their practicality for Closed-Loop Reservoir Management (CLRM), which is inherently dependent on rapid iterative simulations for real-time model updating and operational decision-making. Although physics-based data-driven flow-network models, such as General-Purpose Simulator-powered Network model (GPSNet), can accelerate simulations, their lack of geological constraints compromises predictive reliability. To address this limitation, we propose a novel facies-constrained flow-network model (GPSNet-FC) within the GPSNet framework. This model simplifies reservoir geometry into a 1D discretized grid between wells while incorporating sedimentary facies boundaries identified through edge detection and level-set methods. Grid properties are assigned and calibrated based on facies-specific attributes to ensure geological consistency. GPSNet-FC is applied to history matching using the Ensemble Smoother with Multiple Data Assimilation (ESMDA) and to polymer flooding optimization via the Differential Evolution (DE) algorithm. Numerical case studies validate the method, demonstrating that GPSNet-FC outperforms the original GPSNet in both reliability and accuracy. By integrating facies-based geological constraints, this approach reduces non-uniqueness in history matching and enables rapid and accurate decision-making for polymer flooding strategies. This work advances the integration of geological data into physics-based data-driven models, offering a robust and efficient tool for the CLRM of polymer flooding reservoirs.

1. Introduction

Polymer flooding is a key technology for enhanced oil recovery, which is mainly used in high water-cut reservoirs at the later stage of water flooding development (Dong et al., 2024; Fang et al., 2024; Salem et al., 2024a, 2024b; Yan et al., 2024a). This technology increases the viscosity of displacement fluid by injecting high molecular weight polymers, and then enhances sweep efficiency by reducing oil-water mobility ratio and suppressing viscous fingering. Therefore, it can effectively improve the displacement efficiency and oil recovery of heterogeneous reservoirs, especially for those with significant heterogeneity and high water-cut (usually more than 90%) (Xu et al., 2018). To reduce development risk and maximize the benefits of polymer flooding, the CLRM (Hou et al., 2015; Jansen et al., 2009; Nasir and Durlofsky, 2024) including forward modeling, history matching and production optimization is recommended. The traditional CLRM is highly dependent on the full-order numerical simulation with high-fidelity geological model. Despite their ability to accurately reflect complex geological structures and predict displacement dynamics, they also have the following challenges (Ren et al., 2023a): (1) Building a high-fidelity geological model requires a large amount of geological data and multidisciplinary

* Corresponding author.
E-mail addresses: jsyanxia1989@163.com, 20190025@upc.edu.cn (X. Yan).
Peer review under the responsibility of China University of Petroleum (Beijing).

https://doi.org/10.1016/j.petsci.2026.02.004
1995-8226/

collaboration, and the modeling cycle could take weeks to months. (2) A single full-order numerical simulation typically takes hours, and history matching and production optimization may require thousands of numerical simulations, thus it is computationally expensive (Wang et al., 2024; Zhou et al., 2024). These challenges make the CLRM based on full-order numerical simulations impractical in many application scenarios, especially those requiring rapid or large-scale evaluation. Therefore, how to develop the simplified models that reflect the characteristics of reservoir production and can be used to replace full-order numerical simulations to alleviate above challenges is a key point to realize the CLRM of polymer flooding reservoirs.

Recently, a range of surrogate models that can capture the main production characteristics and trends have been developed to be the alternative to the full-order numerical simulation, and they can be broadly classified into three types (Yan et al., 2024c): data-driven, physics-based, and hybrid methods. Data-driven approaches, such as spearman rank analysis method (Griffiths, 1998; Zhang and Wang, 2023), decline curve analysis (Arps, 1945; Tadjer et al., 2022; Tostado et al., 2016; Valkó, 2009), and machine learning models (Bai et al., 2024; Lin et al., 2025; Pan et al., 2021; Wang et al., 2019; Yan et al., 2024b, 2025), have the advantages of high modeling efficiency and wide applicability. Although the feasibility of these methods has been well demonstrated, they still face some challenges in practical applications, such as relying heavily on the quantity and quality of data, which is usually expensive or time-consuming to acquire. When the quantity or quality of data does not meet the requirements, the prediction accuracy of data-driven surrogate models may be significantly reduced. Different from data-driven approaches, physics-based approaches aim to improve computational efficiency by reducing the complexity of full-order numerical simulation models, such as reducing the number of computational grids and simplifying the governing equations. Representative physics-based approaches include but are not limited to upscaling approaches (Durlofsky, 2005; King et al., 1998; Wen and Gómez-Hernández, 1996; Zhang et al., 2021), multi-scale approaches (Cai et al., 2024; Tchelepi et al., 2007), streamline-based models (Datta-Gupta and King, 2007; Rao et al., 2024), fast-matching approaches (Li and King, 2020; Li et al., 2021), and reduced-order models (He, 2013; Kadeethum et al., 2022; Zalavadia et al., 2019). Although these physics-based approaches do not rely on the quantity and quality of data, they are based on the full-order numerical simulation with high-fidelity geological model. In hybrid methods, some geological information and flow mechanisms are used to build physics-based simplified models, and these simplified models after rapid calibration using observed/simulated data can maintain credible predictions compared to full-order numerical simulation. Therefore, hybrid methods are also known as physics-based data-driven and possess the strengths of the first two types. One representative hybrid method is the Capacitance-Resistive Model (CRM) (Yousef et al., 2006), which can offer more reliable predictions of reservoir dynamics as it is based on the material balance equation. The CRM has been successful in quite a few field applications (Cao et al., 2014; Naudomsup and Lake, 2019; Parekh and Kabir, 2013; Yewgat et al., 2022). However, it has some limitations due to its over-simplifications, such as, the allocation factors and productivity indices of production wells are assumed to be constant the production phase, however they both usually change significantly as the production operation changes in reality. Besides, the bottom hole pressure controls are not allowed in CRM during the production prediction and optimization process (Guo et al., 2018). To alleviate these limitations, the Inter-Well Numerical Simulation Model (INSIM) (Zhao et al., 2016) and its variants (Du et al., 2025; Grave et al., 2024; Guo and Reynolds, 2019; Guo et al., 2017, 2018; Li et al., 2023; Li and Onur, 2023; Zhao et al., 2020, 2021) were proposed, and they have achieved satisfactory performance in conventional water flooding reservoirs. However, these INSIM family models cannot be applied for the numerical simulations with strong nonlinear characteristics, such as chemical flooding and steam flooding, as they are based on semi-analytical approaches (Rao et al., 2021; Ren et al., 2023a). In response to this challenge, some hybrid models based on numerical methods were proposed, for instance, Flow-Network Model (Lerlertpakdee et al., 2014), FlowNet framework (Kiærr et al., 2020; Leeuwenburgh et al., 2024), StellNet model (Lutidze, 2018), and GPSNet (Guan et al., 2024b; Ren et al., 2019; Ren et al., 2023a; Wang et al., 2022; Wang et al., 2021). Among these models, GPSNet uses commercial simulators to carry out numerical simulations of Flow-Network model, thus it has great potential in dealing with practical complex problems, such as large-scale model (Ren et al., 2023b) and steam flooding model (Wang et al., 2022). However, current GPSNet still has some limitations. Firstly, GPSNet does not consider the sedimentary facies constraints in history matching. When sedimentary facies constraints are not considered, even if the fitting accuracy is high, the calibrated model may still not match the actual geological features due to the inherent non-uniqueness of history matching, and then its prediction. Moreover, although the GPSNet framework has shown satisfactory performance in conventional waterflooding applications, its applicability to polymer flooding remains uncertain. Unlike waterflooding, polymer flooding modifies the viscosity of the injected phase, resulting in a significantly altered mobility ratio and enhanced sweep efficiency (He et al., 2024). Furthermore, polymer injection involves additional physicochemical processes such as polymer adsorption, retention, and shear degradation, which introduce stronger nonlinearities into the flow dynamics (Wang et al., 2025). These mechanisms are not explicitly accounted for in the original GPSNet formulation, raising doubts about whether its simplified representation of interwell connections can accurately capture the complex behavior of polymer flooding.

In this study, we adopt GPSNet framework to establish a facies-constrained flow-network model (GPSNet-FC) for fast history matching and production optimization of polymer flooding reservoirs. Specifically, we use the edge detection method, which is based on level-set function (Osher and Fedkiw, 2001), to identify the boundaries between different facies in a sedimentary facies map, and then initialize the GPSNet-FC model according to the identified facies distribution and the attributes of each facies to ensure that the initial model aligns well with the actual geological understanding. After that, the history matching based on the ESMDA (Emerick and Reynolds, 2013) algorithm is carried out to calibrate the flow-network model, meanwhile the sedimentary facies constraints are added to ensure that the calibrated model matches production data while respecting geological features. Finally, based on the calibrated model and considering the main mechanism of polymer flooding, we set up the optimization method of polymer flooding by using the DE algorithm (Das and Suganthan, 2010; Shen et al., 2024) with Net Present Value (NPV) as the optimization objective.

The remaining content of this paper is as follows: Firstly, a brief overview of the GPSNet framework and the details of GPSNet-FC model for fast history matching and production optimization of polymer flooding reservoirs are introduced in the Methodology section. Then, the superiority and applicability of the proposed method is demonstrated through some case studies in the Results and Discussions sections. Finally, the main contents of this study and the further work are summarized in the Conclusions section.

2. Methodology

2.1. Overview of GPSNet framework

This section provides a concise review of the GPSNet framework modeling process; for more comprehensive details, readers are encouraged to consult previous studies (Ren et al., 2019; Ren et al., 2023b; Wang et al., 2022; Wang et al., 2021).

The construction of the GPSNet framework involves four main steps, as shown in Fig. 1. Initially, the perforation and completion intervals are determined. Then, a flow network is constructed based on well locations and completion information. Subsequently, this network is geometrically mapped onto a 2D Cartesian coordinate system through coordinate transformation, enabling seamless coupling with commercial numerical simulators (we use Eclipse in this study). Finally, the model is parameterized for characterization, where key reservoir properties are assigned.

2.1.1. Determine perforation and completion intervals

We can define the discrete perforation intervals based on the well-completion information. Fig. 2 illustrates the process of dividing the wellbore into four perforation intervals. The completion sections (denoted by red pipes) are initially concatenated and then evenly divided into several segments, with a well-point placed at the center of each segment (marked by yellow dots). Subsequently, the well point positions are mapped back to the original well trajectory. In this study, vertical barriers, stacked reservoir zones, and vertically separated perforations were not considered. Therefore, according to the findings of (Guan et al., 2024a), placing a single well point along each vertical well trajectory is sufficient. Fig. 2 illustrates an example with four well points mainly for demonstration purposes—to show that multi-node configurations can also be accommodated within the GPSNet framework and to remain consistent with the original schematic in Wang et al. (2021).

2.1.2. Building connection diagram

In this study, the reservoir models feature relatively complete well patterns with moderate well spacing and no major structural complexities such as faults or fractures. Therefore, the constructed flow networks only employ connections between existing well points, which are sufficient to represent the primary flow pathways. In more complex geological settings, such as reservoirs with extensive fracture networks or irregular boundary conditions, it may become necessary to introduce additional nodes. These can include boundary nodes or virtual well points (with zero injection/production rates) to better capture lateral flow and improve the physical representativeness of the flow system (Kiærr et al., 2020).

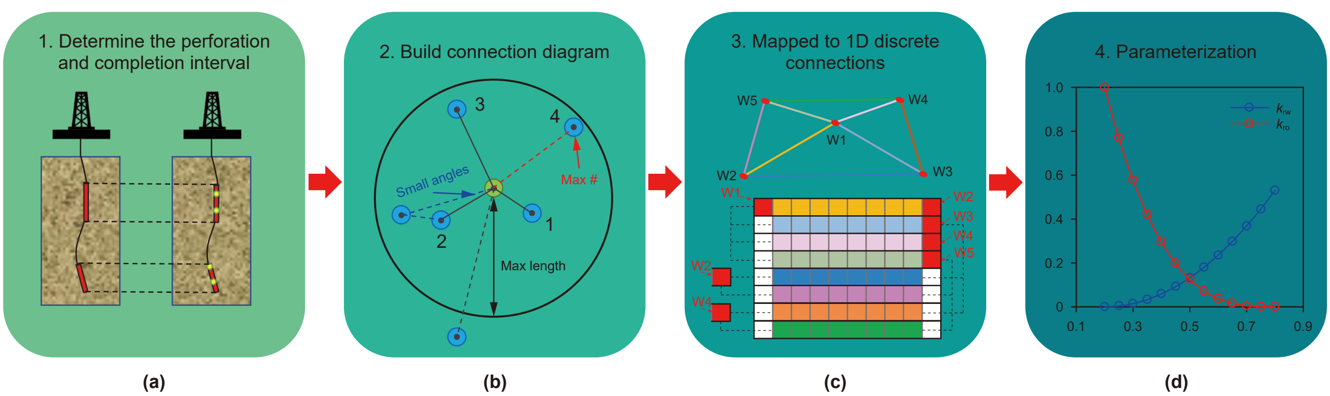

Fig. 1. Steps for Constructing the GPSNet framework. **(a)** Determine the perforation and completion interval. **(b)** Building connection diagram. **(c)** Mapped to 1D discrete connections. **(d)** Parameterization, where k_{ro} and k_{rw} represent the relative permeabilities for oil and water, respectively.

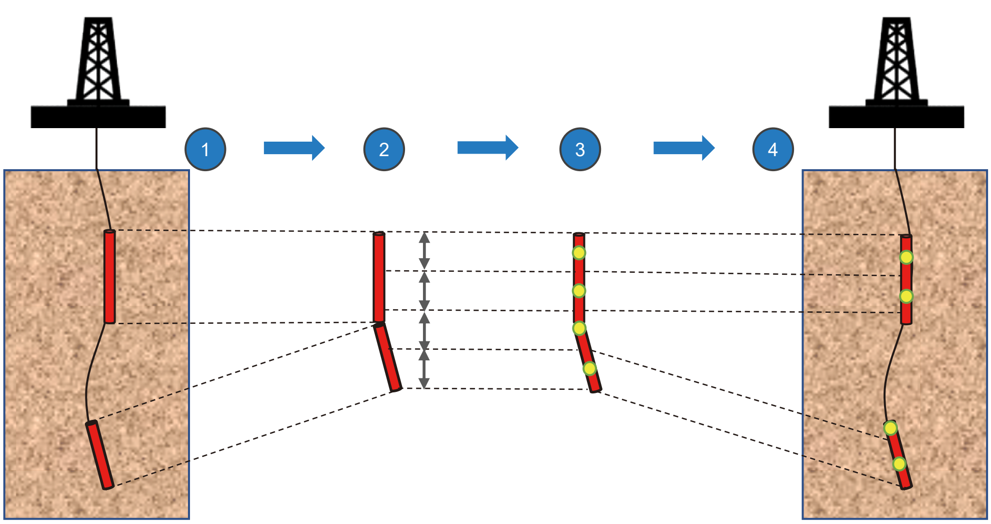

Fig. 2. Discretization of discontinuous completions along a wellbore with four well points. Black curves show the well-trajectories, red cylinders show effective completions, and yellow dots indicate the well points (Wang et al., 2021).

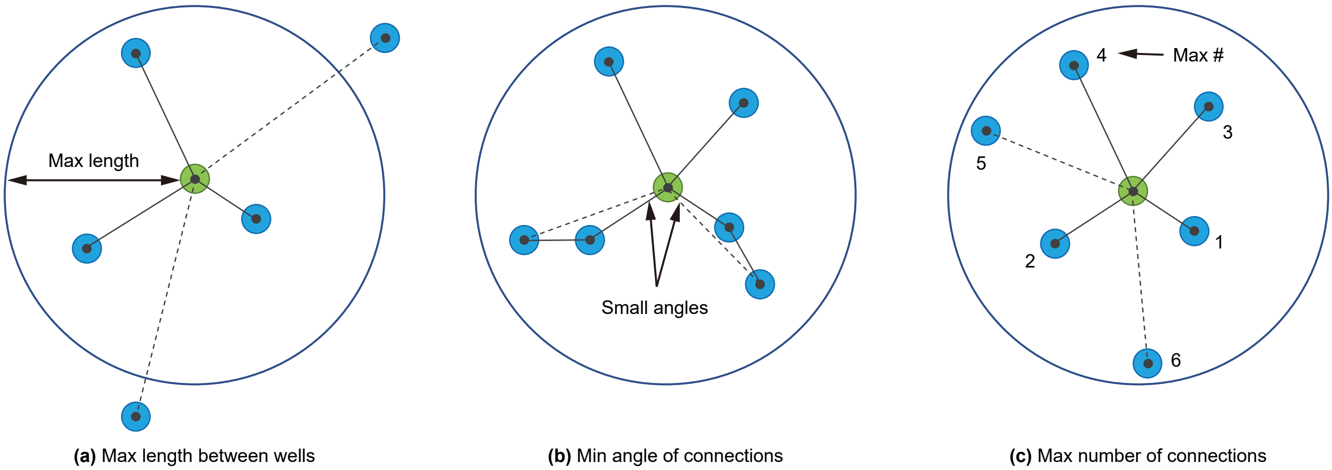

Fig. 3. Criteria for flow network generation of GPSNet. **(a)** Max length between wells. **(b)** Min angle of connections. **(c)** Max number of connections (Wang et al., 2021).

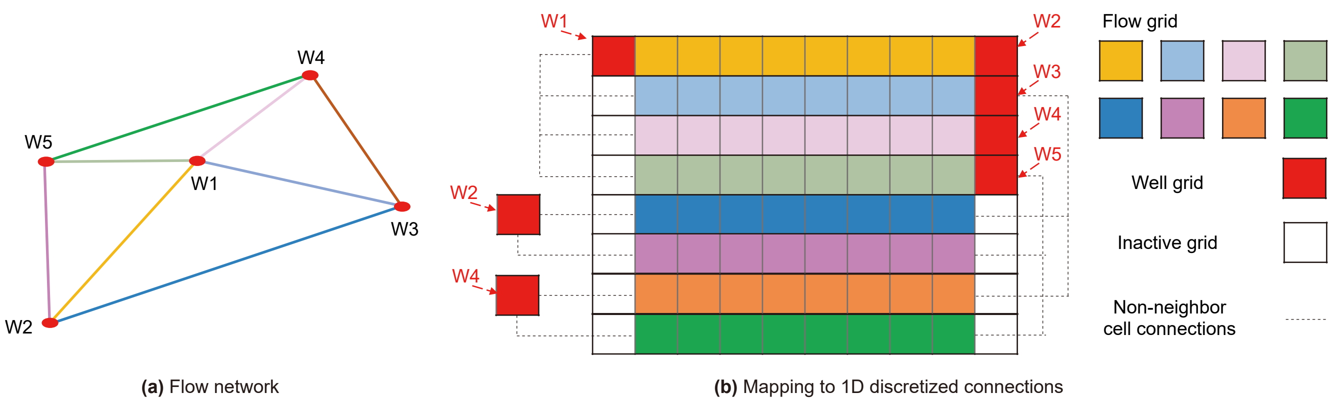

Fig. 4. Mapping flow network to a series of 1D discretized connections. **(a)** Flow network. Red dots represent wells, and lines show the connections between wells. **(b)** Mapping to 1D discretized connections. Red grids are well grid cells, white grids are inactive grid cells, and other grids are flow grid cells. Grids separated by gray solid lines allow flow, while those separated by black solid lines do not, which means that the grid between the different connections does not allow flow. Dashed lines indicate non-adjacent connections (Ren et al., 2023).

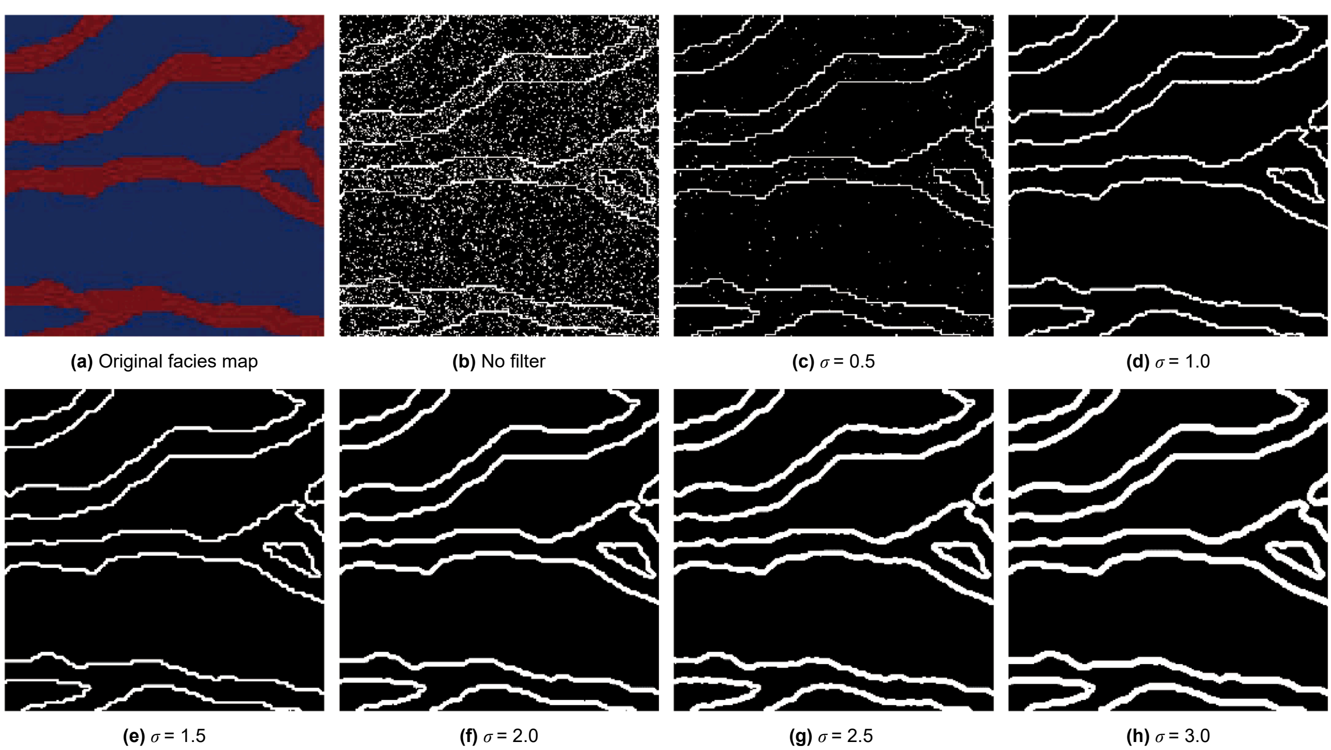

Fig. 5. Sensitivity analysis of the Gaussian filter parameter σ on facies boundary detection. **(a)** Original facies map. **(b)** No Gaussian filtering, showing fragmented edges caused by local noise. **(c)–(h)** Edge detection results obtained with different Gaussian filter parameters (σ = 0.5, 1.0, 1.5, 2.0, 2.5, and 3.0).

The GPSNet framework employs 1D finite difference grids to replace the traditional grid system used in numerical simulations, making the construction of the flow network a critical component. Wang et al. (2021) introduced three selectable parameters (maximum length $l_{\max}$, minimum angle $\theta_{\min}$, and maximum number of connections $n_{c,\max}$) to filter the connections between wells for forming the initial flow network, as shown in Fig. 3. Taking a central well point (green well) as an example, when the distance between two wells exceeds $l_{\max}$, it is assumed that the two wells are not connected, and the connection is removed, as shown in Fig. 3(a). When the triangle formed by three wells has an internal angle smaller than $\theta_{\min}$, the two furthest wells are considered to be connected indirectly through the intermediate well, and the longest connection is removed, as shown in Fig. 3(b). If the number of selectable connections for a well exceeds $n_{c,\max}$, only the $n_{c,\max}$ closest connections are retained, as shown in Fig. 3(c), where the connection between green well and well 5 and well 6 is deleted. Certainly, in GPSNet, all connections can be manually adjusted based on prior knowledge and geological understanding. The connectivity graph can be modified after applying the three parameters to more accurately describe the primary flow pathways in the subsurface reservoir.

2.1.3. Map the flow network to 1D discrete connections

Most commercial numerical simulators operate on grids in Cartesian coordinate systems. To ensure compatibility with traditional reservoir simulators (such as those based on finite difference or finite volume methods), Ren et al. (2019) mapped the connectivity graph constructed above to a 1D discrete grid cells that can be recognized by commercial numerical simulators, as shown in Fig. 4. For example, in a five-point well network, there are five well points and eight connections. Fig. 4(b) shows the mapped 1D connection graph, where the red blocks represent the well point grid cell, located at the two ends of the mapped graph. The colored blocks in the middle correspond to the connections of the same color in Fig. 4(a) and represent the flow grid cells. Clearly, the number of well grid cells exceeds the number of well points, so non-adjacent connections are used to link the well points to the flow paths (dashed lines represent non-adjacent connections), while redundant grid cells are set as inactive (white grid cells) and are not included in the simulation calculations. There are impermeable barriers between different connections (black solid lines), representing zero permeability in the y-direction or inactive grid cells placed between the connections. The gray solid lines represent transmissible interfaces. Ren et al. (2019) suggested that employing 10 grid cells can achieve an optimal trade-off between computational speed and accuracy during traditional waterflood simulations. However, for scenarios involving polymer flooding or other chemical-enhanced oil recovery techniques, which experience highly diffusive flow behavior, 10 grid cells are often insufficient to meet the required computational accuracy. In this study, we set the number of grid cells in the connections to 25 (including the well grid cells) to better capture the detailed representation of depositional facies.

2.1.4. Model parameterization

The parameterization process of the GPSNet primarily relies on well log and completion data, and takes the average value of the well point properties at both ends of the connection as the initial value of the grid properties in the connection. This approach provides a simple and rapid way to establish the model's initial state. However, according to this study, the subsequent prediction results based on this assignment method are unreliable. This is because history matching is an ill-posed problem with multiple solutions. Without the addition of constraints, the fitting process will search across the entire parameter space. Although the final fit may appear satisfactory production performance, the resulting parameter field can diverge significantly from the true values and fail to correspond with geological interpretations, thereby compromising predictive performance. In this section, we first introduce the parameters that need to be determined for the GPSNet and the items directly influenced by these parameters.

Capillary pressure: phase pressure, phase distribution.

Relative permeability model parameters: phase rate, phase distribution.

Water-oil contact (WOC) depth: phase distribution.

Rock compaction, fluid compressibility, fluid pressure, volume, temperature (PVT): phase volume, phase rate.

Reservoir pressure/temperature: well performance, fluid PVT.

Grid permeability: phase rate.

Grid volume: phase volume.

Producer/injector well index (WI): well performance.

The reasonable assignment of grid-cell volumes is as important as the allocation of permeability, since cell volume directly determines the phase capacity of each grid cell. However, in practice, the prior information required for “informed” grid-volume assignment is usually unavailable, making it difficult to define accurate volume distributions directly from geological data. Therefore, we generated the prior grid volumes uniformly in this work, and to ensure physical reasonableness, the total volume was constrained during the history-matching process. For two-phase oil-water flow, the Corey model (Brooks, 1965) is used to describe the relative permeability curves:

$$k_{\mathrm{ro}} = k_{\mathrm{ro}}^{0}\left(\frac{S_{\mathrm{o}} - S_{\mathrm{or}}}{1 - S_{\mathrm{or}} - S_{\mathrm{wr}}}\right)^{N_{\mathrm{o}}}, \quad k_{\mathrm{rw}} = k_{\mathrm{rw}}^{0}\left(\frac{S_{\mathrm{w}} - S_{\mathrm{wr}}}{1 - S_{\mathrm{or}} - S_{\mathrm{wr}}}\right)^{N_{\mathrm{w}}} \tag{1}$$

where k_{ro}^{0} and k_{rw}^{0} represent the endpoint relative permeabilities for oil and water, respectively, N_{o} and N_{w} control the curvature of the oil and water relative permeability curves, S_{or} is the residual oil saturation, and S_{wr} is the irreducible water saturation.

2.2. Facies-constrained GPSNet model

To enhance the reliability of the GPSNet framework during the prediction stage, it is essential to integrate more geology-related prior knowledge to reduce the randomness of history matching solutions. In field practice, the most effective geological data to describe the distribution of subsurface sand bodies are depositional facies maps. Therefore, in this study, the GPSNet framework is improved by proposing the GPSNet-FC model, which incorporates depositional facies information into the modeling process. In this study, the available facies data are provided as a pixel-based image rather than a grid-aligned model that directly corresponds to the simulation grid. Therefore, a series of preprocessing steps are applied to ensure accurate facies mapping. Specifically, Gaussian filtering is used to remove high-frequency noise and improve the continuity of facies boundaries; the Sobel operator is employed to detect boundary gradients between different facies; and the level set method is employed to evolve and smooth the detected boundaries into continuous and closed interfaces $\phi(x, y)$ whose sign distinguishes different facies regions. The processed depositional facies map is then integrated with the GPSNet model, enabling grid cells associated with different facies to be assigned property values according to the attributes of their respective facies. This procedure allows the initial model to better conform to the geological characteristics of the reservoir. The details of the GPSNet-FC model are as follows:

2.2.1. Edge detection

We use edge detection (Torre and Poggio, 1986) methods to identify the initial boundaries of sedimentary facies. The edge of an image refers to areas where there is a significant change in pixel intensity within a localized region. In digital images, these edges manifest as abrupt transitions in grayscale values, resulting in local discontinuities that delineate distinct structural features. Depositional facies maps illustrate the spatial distribution of a reservoir's depositional environments and rock types, providing insights into the relationships between different facies. These maps typically feature distinct facies boundaries, which are particularly prominent in fluvial depositional systems. Edge detection techniques can be effectively applied to identify and delineate these facies boundaries, enhancing the accuracy of facies classification.

First, the obtained depositional facies map is converted into a grayscale image. A Gaussian filter is then applied to denoise the image, which works by performing a weighted average based on the grayscale values of the pixel to be filtered and its surrounding neighborhood. This method effectively filters out high-frequency noise superimposed on the image, ensuring that the gradient computation reflects genuine geological transitions rather than random pixel variations. The Gaussian function is as follows:

$$f(x,y)=\frac{1}{2\pi\sigma^2}e^{-\frac{x^2+y^2}{2\sigma^2}} \tag{2}$$

where σ is the parameter that controls the standard deviation of the Gaussian filter.

We use the Sobel operator to calculate the first derivative and identify the points where the grayscale values change most rapidly, thereby determining the image edges. Compared with a simple 1D two-cell filter, the Sobel operator provides better noise tolerance and directional sensitivity, which helps capture continuous boundary features even when the image contains minor pixel irregularities. The Sobel operator convolves the image with convolution kernels in the X and Y directions to compute the gradient value for each pixel. The gradient value is then compared with a given threshold $T_{\text{threshold}}$; if it exceeds the threshold, the point is considered an edge point. The convolution kernels in the X and Y directions, $Sobel_x$ and $Sobel_y$, are as follows:

$$Sobel_x=\begin{bmatrix}-1 & 0 & 1\\ -2 & 0 & 2\\ -1 & 0 & 1\end{bmatrix} \tag{3}$$

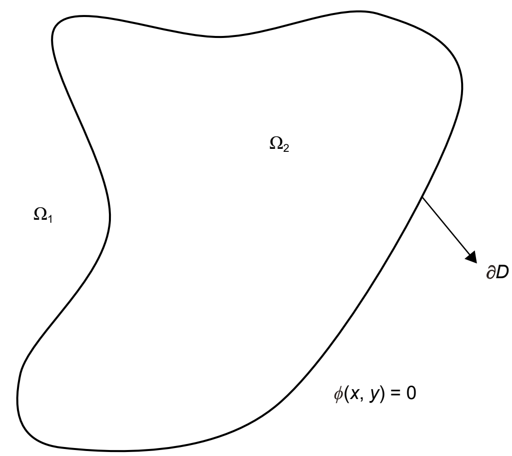

Fig. 7. The level set function differentiates sedimentary facies.

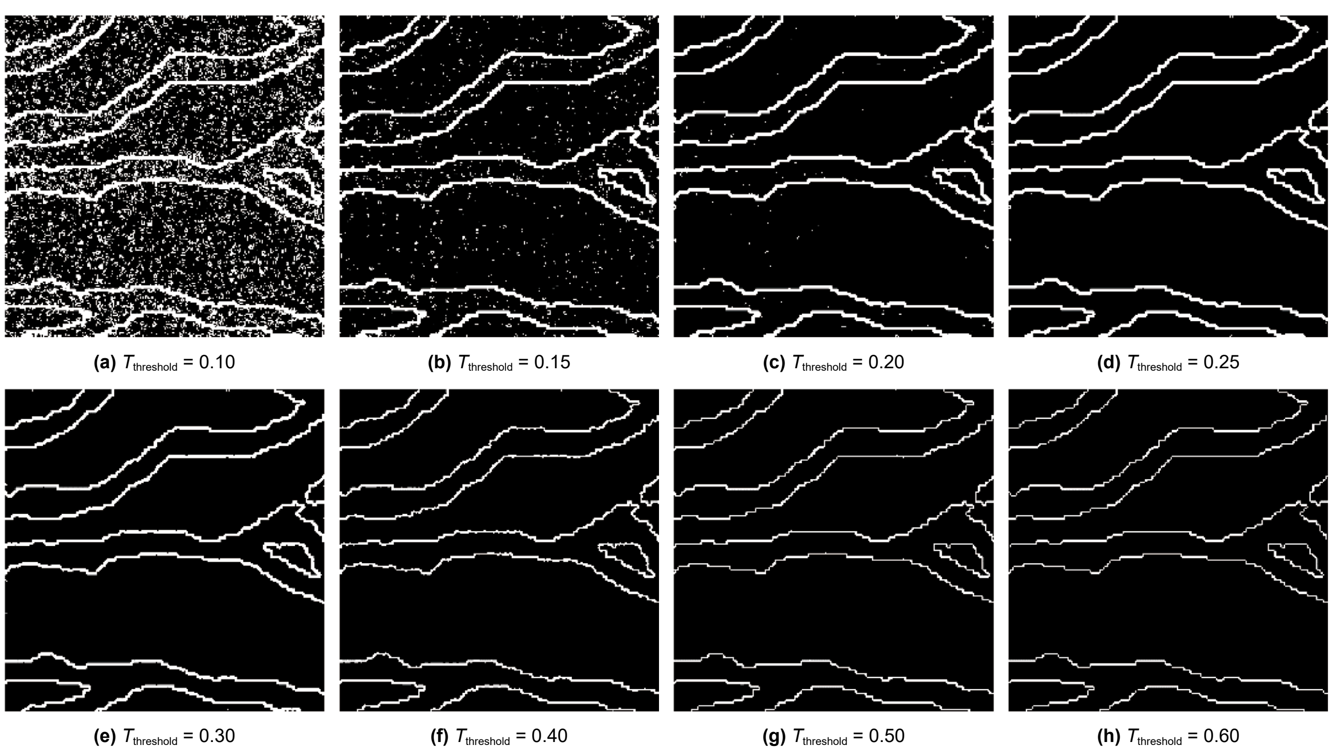

Fig. 6. Sensitivity analysis of the Sobel threshold $T_{\text{threshold}}$ on sedimentary facies boundary detection. The Gaussian filter parameter was fixed at $\sigma = 1.5$. **(a)**–**(h)** Edge detection results obtained with different Sobel threshold ($T_{\text{threshold}}$ = 0.10, 0.15, 0.20, 0.25, 0.30, 0.40, 0.50 and 0.60).

$$Sobel_y = \begin{bmatrix} -1 & -2 & -1 \\ 0 & 0 & 0 \\ 1 & 2 & 1 \end{bmatrix} \tag{4}$$

If A is the original image, the gradient magnitudes in the horizontal and vertical directions G_x and G_y, are as follows:

$$G_x = Sobel_x \times A \tag{5}$$

$$G_y = Sobel_y \times A \tag{6}$$

The total gradient G for each pixel is given by:

$$G = \sqrt{G_x^2 + G_y^2} \tag{7}$$

The gradient direction θ is given by:

$$\theta = \tan^{-1}(G_x / G_y) \tag{8}$$

To evaluate the influence of parameter selection on facies boundary extraction, sensitivity analyses were conducted for both the Gaussian filter parameter σ and the Sobel threshold $T_{\text{threshold}}$. As shown in Fig. 5, the sedimentary facies maps used in this study often contain minor local noise that can generate fragmented edges when no Gaussian denoising is applied. We tested a range of Gaussian filter parameters (σ = 0.5, 1.0, 1.5, 2.0, 2.5, and 3.0) to examine their effects on edge continuity. The results indicate that when $\sigma > 1.0$, the extracted boundaries become clearer and more continuous. A larger σ provides stronger denoising capability but may also smooth fine details. The optimal σ value depends on image quality and noise level; since the sedimentary facies maps in this study exhibit well-defined and distinct facies boundaries, a relatively large σ (1.0–3.0) is appropriate for effective denoising while preserving edge geometry.

For the Sobel operator, a fixed threshold approach was adopted because facies maps consist of only a few distinct color regions with sharp contrast, resulting in most pixels having near-zero gradient magnitudes within homogeneous zones. According to (Jähne, 2005), for images with clear edges and low noise, a single fixed threshold is often sufficient for reliable edge detection. In the sensitivity test, the Gaussian filter parameter was fixed at σ = 1.5, while the Sobel threshold was varied from 0.10 to 0.60. The results (Fig. 6) show that small thresholds (e.g., 0.10–0.20) produce noisy and over-sensitive edge maps, whereas larger thresholds (0.30–0.60) suppress weak responses and yield thin and continuous facies boundaries. Therefore, in this study, a threshold in the range of 0.30–0.60 was selected as optimal for sedimentary facies boundary identification.

2.2.2. Level set method

Edge detection can effectively highlight facies boundaries, but it is highly sensitive to noise, often producing fragmented or discontinuous edges and yielding a discrete, pixel-based contour. Such contours neither provide a continuous mathematical representation of the boundary nor define which region is which facies, so they cannot be directly used to assign facies types on the simulation grid. We therefore use the edge map only to initialize a level set function and then evolve it to obtain clean, continuous, and closed boundaries together with an explicit region labeling.

The core idea of the level set method is to use a high-dimensional scalar function (i.e., the level set function) to represent the position and shape of a surface without explicitly describing the surface. Typically, the signed Euclidean distance from a point on the plane to the contour curve is chosen as the level set function (Osher et al., 2004). Suppose the reservoir's depositional model is divided into two depositional facies, Ω_1 and Ω_2, with a closed curve ∂D serving as the boundary between the two facies. Each depositional facies is represented by its corresponding geological parameters, as shown in Fig. 7. The level set function corresponding to the point (x, y) in the image should be:

$$\phi(x, y) = \begin{cases} d[(x, y), \partial D] & (x, y) \in \partial D \\ -d[(x, y), \partial D] & (x, y) \notin \partial D \end{cases} \tag{9}$$

where $d[(x, y), \partial D]$ is the distance from the point (x, y) to the level set contour curve ∂D. The distance is positive inside the curve, zero on the curve, and negative outside the curve.

The level set function, evolving over time, can be denoted as $\phi_i(x, y, t)$. The evolution of the surface is typically described by the core equation of the level set method (the level set evolution equation):

$$\frac{\partial \phi_i}{\partial t} + \frac{\partial D_{ij}}{\partial t} |\nabla \phi_i| = 0 \tag{10}$$

where $\partial D_{ij}/\partial t$ is the velocity function, which determines the direction and speed of the surface evolution between facies i and j, and $|\nabla \phi_i|$ represents the gradient magnitude of the level set function.

After the evolution, we obtained a numerical representation of the mathematical curve $\phi\left(x_{\text{img}}, y_{\text{img}}\right)$, because the facies image and the simulator use different coordinate systems, we apply a simple linear mapping:

$$x_{\text{sim}} = a_x x_{\text{img}} + b_x,\ y_{\text{sim}} = a_y y_{\text{img}} + b_y \tag{11}$$

where x_{sim} and y_{sim} are the coordinates of the grid cells, x_{sim} and y_{sim} are the pixel coordinates, a_x and a_y are the scale factors, b_x and b_y are the offset terms. By evaluating the evolved level set function ϕ at $(x_{\text{sim}}, y_{\text{sim}})$ on the flow-network grid, facies boundaries defined in image space are seamlessly integrated into the simulation domain, ensuring consistent facies-based property assignment in the numerical model.

When more than two facies are present, multiple level set functions can be used. For three facies, for example, two functions ϕ_1, ϕ_2 are sufficient, the sign combination identifies each facies:

Facies A: ($\phi_1 > 0$, $\phi_2 > 0$), facies B: ($\phi_1 > 0$, $\phi_2 < 0$), facies C: ($\phi_1 < 0, \phi_2 > 0$).

Each level set function evolves independently, allowing multiple facies interfaces to be captured simultaneously without explicit tracking of their topological changes.

We randomly generated a set of depositional facies maps using Stanford Geological Statistical Modeling Software (SGeMS, Remy, 2009), as shown in Fig. 8 The facies boundaries were then identified using a combination of edge detection and the level set function, with the results shown in Fig. 9. It is evident that the facies boundaries of each depositional facies map are accurately identified, enabling the segmentation of different geological regions within the reservoir. Based on the GPSNet framework and Sedimentary facies identification, we assigned values to the grid cells according to their corresponding depositional facies types, resulting in the GPSNet-FC model. Even though depositional facies were considered in the initial modeling, the simulation results of the model do not always match the observed data. Therefore, our best approach is to use these values as reference points and further calibrate the model through the History Matching process.

2.3. History matching

There are many data assimilation methods used for parameter calibration, such as gradient-based algorithms (Jacquard, 1965), evolutionary algorithms (Paredes et al., 2013), ensemble Kalman filter algorithms (EnKF) (Evensen, 1994), and Ensemble Smoother with Multiple Data Assimilation (ESMDA) (Emerick and Reynolds,

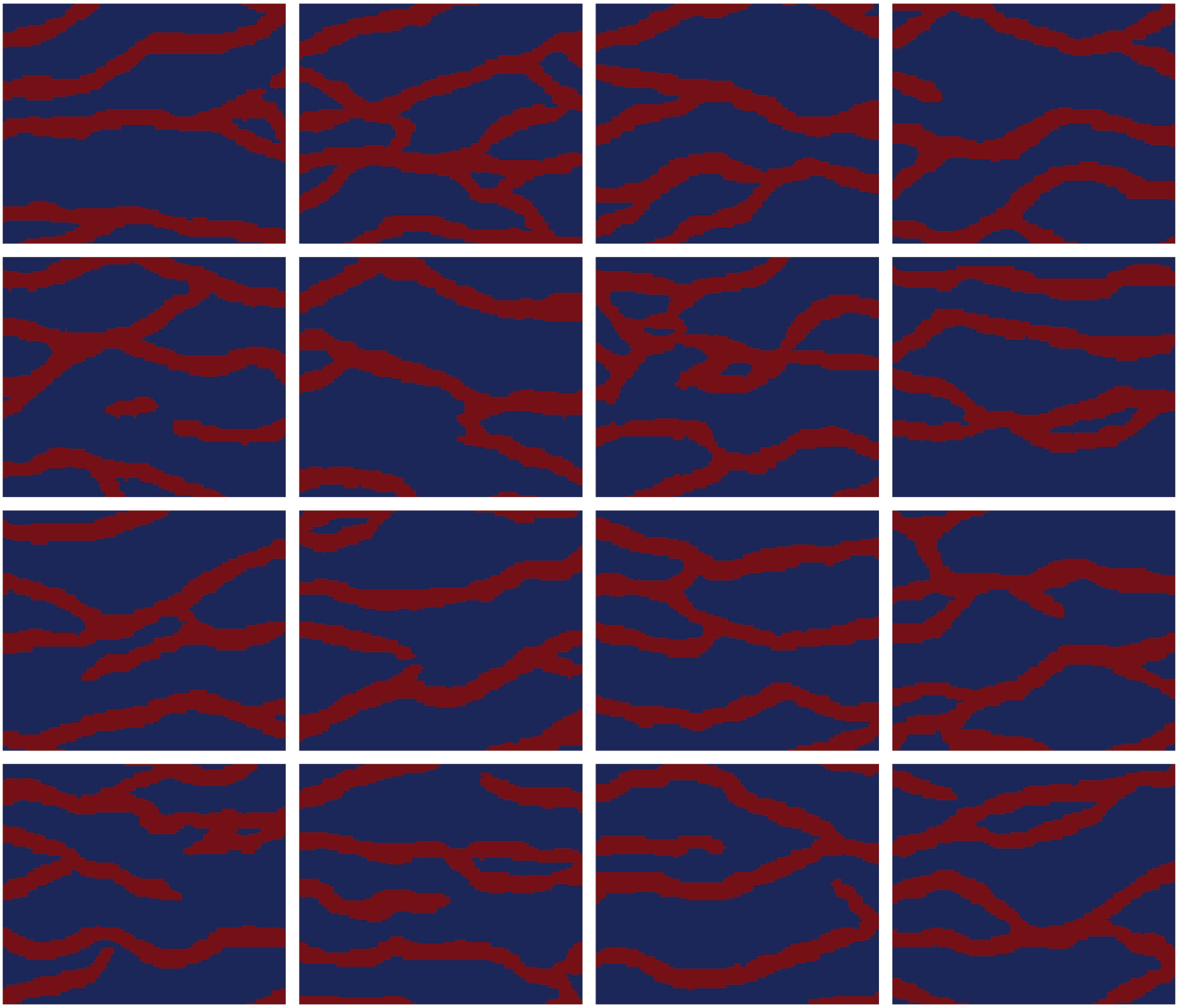

Fig. 8. Sixteen randomly generated sedimentary facies maps. Red channels and blue background representing two different facies.

2013). Where gradient-based algorithms are the most common solution method, which calculate the gradient of the objective function with respect to model parameters and update the parameters along the direction of the gradient, gradually optimizing the model to fit the observed data. However, these methods are challenging to implement, and the convergence process can be very difficult. Evolutionary algorithms simulate the process of biological evolution, including operations such as crossover, mutation, and selection among individuals in a population, gradually evolving solutions with higher fitness to optimize model parameters. As reservoir models become more complex, the slow convergence of evolutionary algorithms has become more pronounced, and with the emergence of other history matching algorithms, evolutionary algorithms are increasingly being rendered obsolete in history matching tasks. EnKF is a Monte Carlo-based filtering algorithm, which uses an ensemble to simulate the probability distribution of a multi-dimensional system and updates the system's state by integrating observational data and model predictions. This method achieves high computational efficiency and is widely used for automatic history-matching tasks. ESMDA is an extension of the EnKF and has been shown to provide greater robustness and accuracy for parameter estimation problems (Emerick and Reynolds, 2013). Moreover, Evensen (2018) has demonstrated the applicability of ESMDA in handling strongly nonlinear systems. Therefore, ESMDA is adopted in this study for the history-matching process.

In the GPSNet-FC model, the main adjustable parameters include the grid volume, grid permeability, and relative permeability, among others. Specifically, the parameter vector m_j can be expressed as:

$$m_j = \left(K_i, ..., V_i, ..., k_{\mathrm{ro}}^0, k_{\mathrm{rw}}^0, N_{\mathrm{o}}, N_{\mathrm{w}}\right)_j \tag{12}$$

where the subscript j represents the sample index, the subscript i represents the grid index, K is the permeability, V is the grid volume, k_{ro}^0 and k_{rw}^0 represent the endpoint values of the oil and water

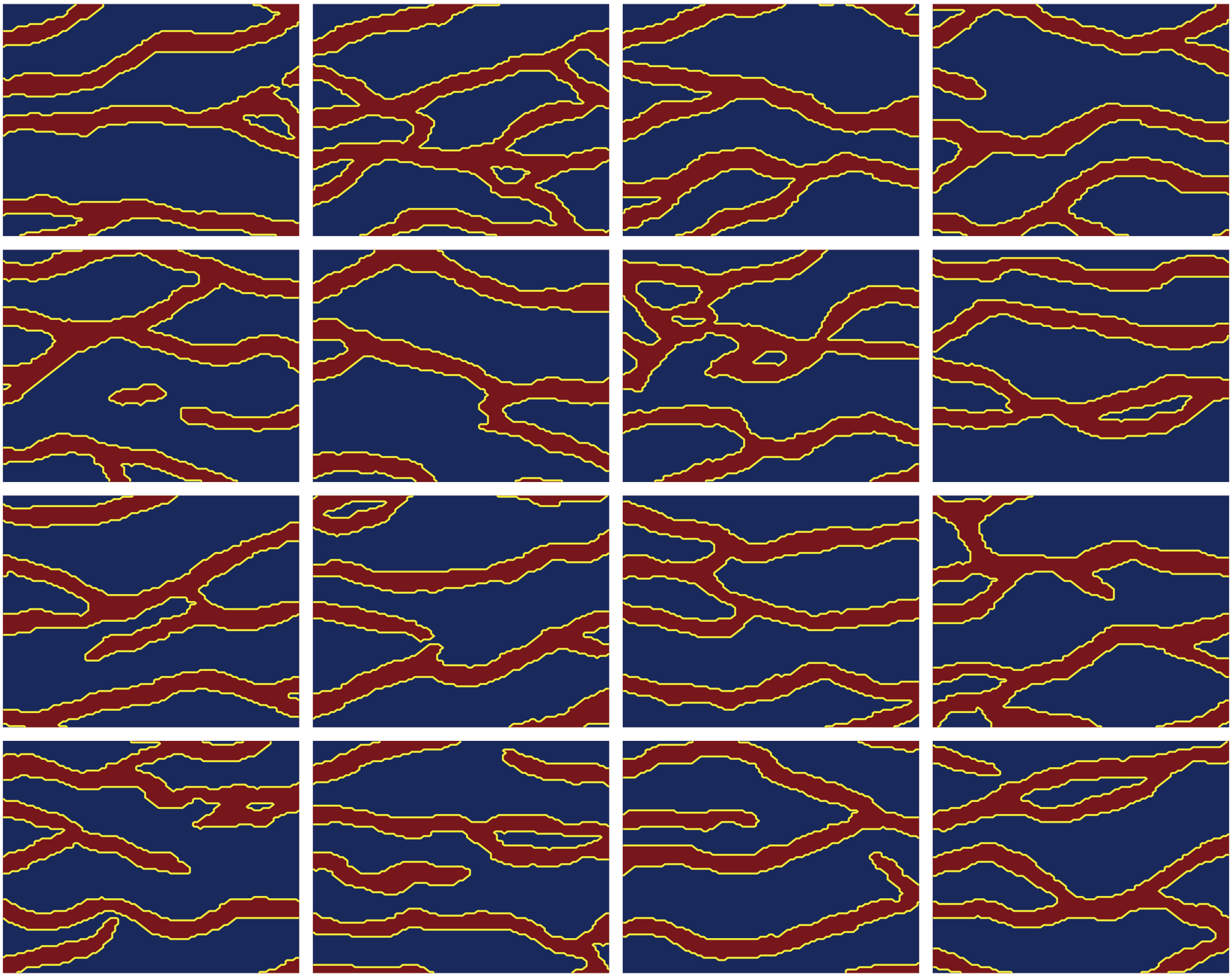

Fig. 9. Identified sedimentary facies boundaries in Fig. 8. Yellow curves representing facies boundaries.

relative permeability curves, while N_o and N_w control the curvature of the oil and water relative permeability curves, respectively.

The essence of history matching is to adjust the parameters m in order to minimize the difference between the model's simulation results and the actual production data. The objective function during the iterative process can be expressed as:

$$\operatorname{argmin} f(m) = \frac{1}{2}(g(m) - d_{\text{obs}})^{\mathrm{T}} C_{\mathrm{D}}^{-1}(g(m) - d_{\text{obs}}) + \frac{1}{2}(m - m^*)^{\mathrm{T}} C_{\mathrm{M}}^{-1}(m - m^*) \tag{13}$$

where $f(m)$ is the objective function value, $g(m)$ is the model simulation result, d_{obs} is the observed data, C_{D} is the covariance matrix of the observation data error, m is the model parameter vector, m^* is the prior vector, and C_{M} is the prior parameter covariance matrix. Eq. (13) generally consists of two terms. The first term represents the data-mismatch term, which measures the difference between simulated and observed data and ensures that the assimilated model can reproduce the observed production behavior. The second term is the prior-deviation term, which quantifies the deviation of updated parameters from their prior distribution to prevent excessive divergence during the matching process.

For a model parameter vector m_j, with n_m parameters, n_d dimensional observed data, and an N_{e} sized ensemble, the update equation for the model parameters m_j^f in ESMDA is as follows:

$$m_j^a = m_j^f + C_{\mathrm{MD}}^f \left(C_{\mathrm{DD}}^f + \alpha_n C_{\mathrm{D}}\right)^{-1} \left(d_{\mathrm{uc},j} - d_j^f\right) \tag{14}$$

for $j = 1, 2, ..., N_{\mathrm{e}}$, where N_{e} is the ensemble size; the superscript a represents the analysis value, and f represents the prediction value; C_{MD}^f denotes the cross-covariance matrix between the model parameter vector m^f and the model's predicted result d^f; C_{DD}^f denotes the auto-covariance matrix of the model's predicted results d^f; C_{D} represents the covariance matrix of the observation data errors; $d_{\mathrm{uc},j}$ is drawn from $N(d_{\text{obs}}, C_{\mathrm{D}})$; d_{obs} is the observed data; α_n represents the inflation factor in the n-th data assimilation step, with $\alpha_n > 1$ and $\sum_{n=1}^{N_a} \frac{1}{\alpha_n} = 1$, N_a is the total number of iterations. In this study, $N_a = 15$ assimilation steps were performed, with equal inflation factors $\alpha_n = 15$ for $n = 1, 2, ..., 15$. The observation data errors were assumed to have a standard deviation equal to 5% of the measured oil production rate, and C_{D} was constructed accordingly. Specifically, in Eq. (14), C_{MD}^f and $C_{\mathrm{DD}}^f$are as follows:

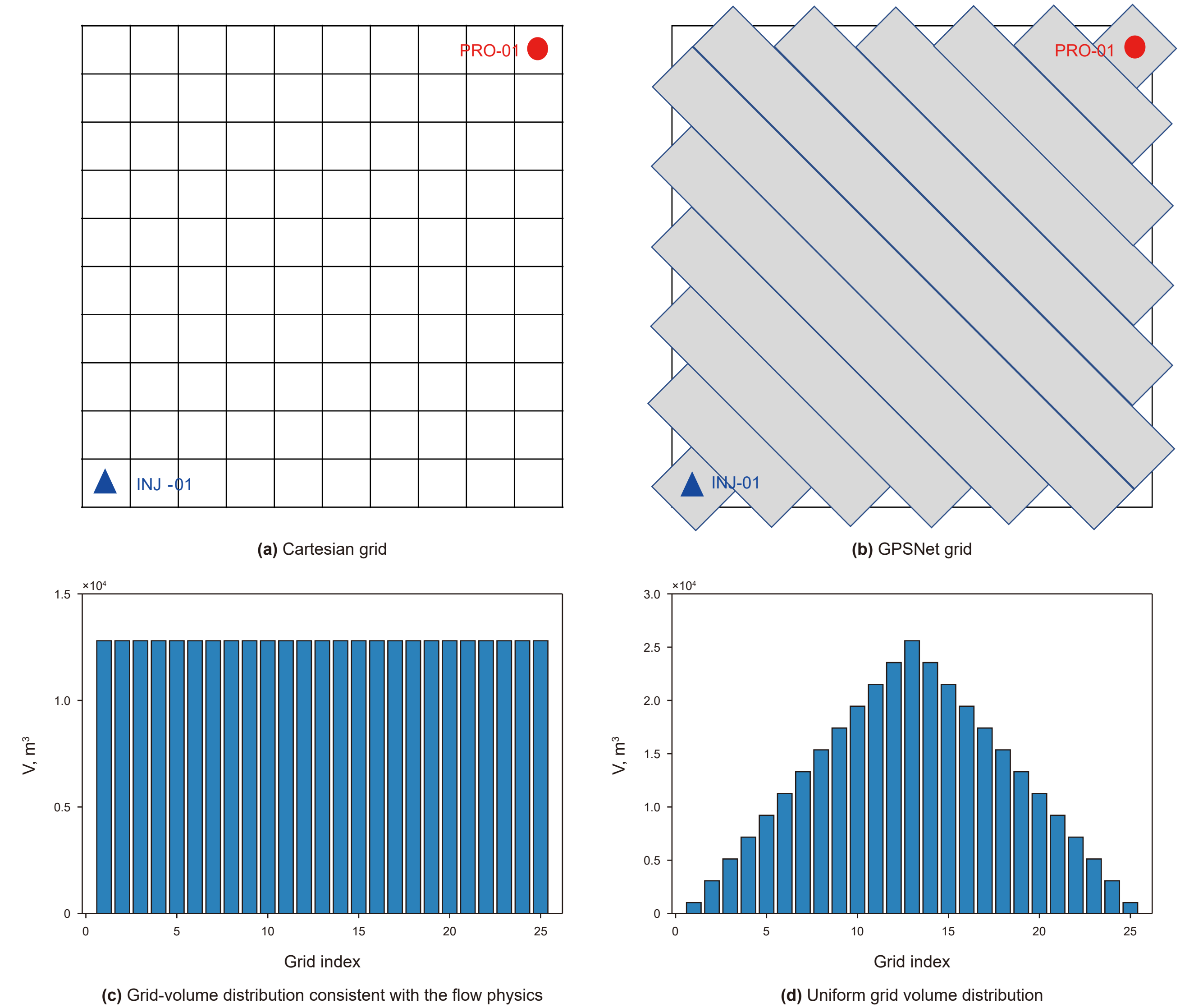

Fig. 10. Reservoir model and grid volume distribution pattern. **(a)** Cartesian grid. **(b)** GPSNet grid. **(c)** Grid-volume distribution consistent with the flow physics. **(d)** Uniform grid volume distribution.

$$\begin{cases} C_{\mathrm{MD}}^{f} = \dfrac{1}{N_e - 1}\sum_{j=1}^{N_e}\left(m_j^f - \overline{m}^f\right)\left(d_j^f - \overline{d}^f\right)^{\mathrm{T}} \\ C_{\mathrm{DD}}^{f} = \dfrac{1}{N_e - 1}\sum_{j=1}^{N_e}\left(d_j^f - \overline{d}^f\right)\left(d_j^f - \overline{d}^f\right)^{\mathrm{T}} \end{cases} \tag{15}$$

where $\overline{m}$ represents the mean value of the prior model parameter vector, and $\overline{d}$ represents the mean value of the model's predicted results. Thus, we have:

$$\begin{cases} \overline{m}^f = \dfrac{1}{N_e}\sum_{j=1}^{N_e} m_j^f \\ \overline{d}^f = \dfrac{1}{N_e}\sum_{j=1}^{N_e} d_j^f \end{cases} \tag{16}$$

During the history matching process, we take two sedimentary facies as examples, Ω_1 and Ω_2. To reduce the randomness in the history matching results and ensure that the model is consistent with the actual geological understanding, we impose constraints on the grid properties and reservoir conditions within each facies:

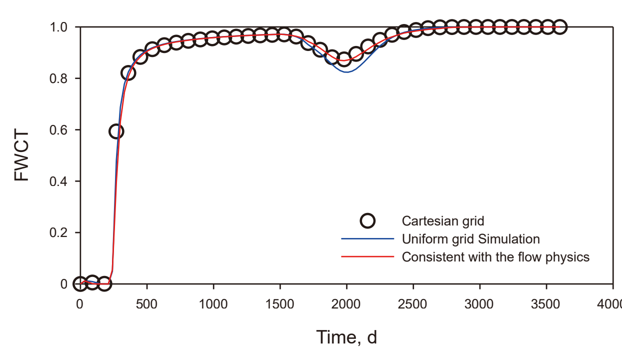

Fig. 11. Comparison of water cut. The black circles represent the results obtained from the Cartesian grid simulation, the red curve corresponds to the GPSNet simulation with a flow-physics-consistent grid-volume distribution, and the blue curve represents the GPSNet simulation with a uniform grid-volume distribution.

$$\begin{cases} K_{\Omega_1\ \min} \le K_{i,\Omega_1} \le K_{\Omega_1\ \max} \\ K_{\Omega_2\ \min} \le K_{i,\Omega_2} \le K_{\Omega_2\ \max} \\ 0 \le V_{i,\Omega_1} \le V_{\Omega_1 \mathrm{tot}} \quad i \in \Omega_1 \\ 0 \le V_{i,\Omega_2} \le V_{\Omega_2 \mathrm{tot}} \quad i \in \Omega_2 \\ \sum_{i=1}^{N_{\Omega_1}} V_{i,\Omega_1} = V_{\Omega_1 \mathrm{tot}} \quad i \in \Omega_1 \\ \sum_{i=1}^{N_{\Omega_2}} V_{i,\Omega_2} = V_{\Omega_2 \mathrm{tot}} \quad i \in \Omega_2 \\ 0 < k_{\mathrm{ro}}^0, k_{\mathrm{rw}}^0 < 1 \\ 1 < N_{\mathrm{o}}, N_{\mathrm{w}} < 6 \end{cases} \tag{17}$$

where $K_{i,\Omega}$ represents permeability of grid i in facies Ω; $K_{\Omega,\min}$ and $K_{\Omega,\max}$ represents the minimum and maximum permeability of facies Ω, respectively; $V_{i,\Omega}$ represents the grid volume of facies Ω; $V_{\Omega_1 \mathrm{tot}}$represents the total reservoir volume of facies Ω; and N_Ω represents the number of grid cells belonging to facies Ω. In our workflow, the prior permeability and grid-volume values were randomly generated within predefined upper and lower limits based on the initial model, and the bounds were defined according to available geological information for each facies, ensuring that all parameter values remain within realistic geological ranges. We noticed that directly applying truncation-based bound constraints to parameter values during the history-matching process may violate the Gaussianity assumption required by the ESMDA formulation. To address this issue, we employ the normal score transform (Jo et al., 2017; Jung et al., 2017) on the model parameters during the history matching process. This procedure preserves the Gaussianity assumption of the ESMDA method while ensuring that the updated parameters remain physically meaningful.

2.4. Production optimization for polymer flooding

The fitted flow network model is regarded as the optimal proxy model and is subsequently used for production optimization of polymer flooding reservoirs. We employ the commercial numerical simulator Eclipse as a numerical solution tool for GPSNet-FC. In Eclipse, polymer flooding is activated using keywords such as “POLYMER”, allowing the simulation to account for various physicochemical processes, including the material balance equation of the polymer solution, adsorption and retention, and shear degradation, and the details can be referred to (Tellez Arellano et al., 2023).

Production optimization aims to obtain the optimal oilfield development strategy by effectively solving the objective function. By adjusting variables such as well control, oil production can be increased while minimizing development costs. In this paper, the NPV is set as the objective function for the production optimization process. Considering the issue of polymer injection, the NPV function is defined as:

$$\max J(u) = \sum_{n=1}^{L} \left[\sum_{j=1}^{N_{\mathrm{P}}} \left(r_{\mathrm{o}} q_{\mathrm{o},j}^n - r_{\mathrm{w}} q_{\mathrm{w},j}^n \right) - \sum_{i=1}^{N_{\mathrm{I}}} r_{\mathrm{wi}} q_{\mathrm{wi},i}^n - \sum_{k=1}^{N_{\mathrm{PI}}} r_{\mathrm{p}} q_{\mathrm{pi},k}^n \right] \frac{\Delta t^n}{(1+b)^{t^n/365}} \tag{18}$$

where, J represents the objective function value, and u denotes the optimization variables, which consist of injection rate, polymer concentration, and liquid production rate. These variables form a parameter vector representing the controllable operation parameters of all wells. L is the total number of control steps. N_{P}, N_{I} and N_{PI} represent the number of production wells, water injection wells, and polymer injection wells, respectively. r_{o}, r_{w}, r_{wi} and r_{p}correspond to the oil price, wastewater treatment cost, water injection price, and polymer injection price, respectively. $q_{\mathrm{o},j}^n$ and $q_{\mathrm{w},j}^n$ represent the average oil production rate and water production rate, respectively, of the production well j at the n-th simulation time step. $q_{\mathrm{wi},i}^n$ is the average water injection rate of the water injection well i at the n-th simulation time step, and $q_{\mathrm{pi},k}^n$ is the average polymer injection rate of the polymer injection well k at the j-th simulation time step. b is the annual discount rate, and Δt^n is the time step length at the n-th simulation time step. $t^n$is the cumulative time up to the n-th simulation time step. The physical meaning of the above equation is the oil revenue minus the costs of water production, water injection, and polymer injection, representing the NPV.

The optimization process is constrained by control boundaries for injection wells and production wells, the range of polymer concentration, and reservoir pressure. The constraints for the optimization process are as follows:

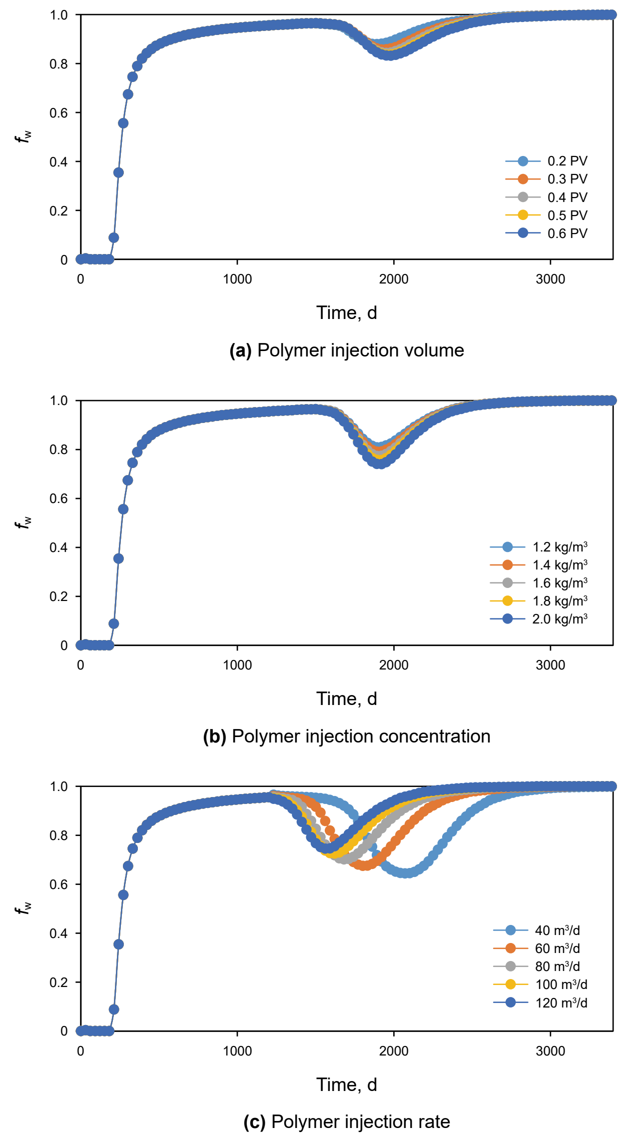

Fig. 12. Sensitivity analysis of polymer parameters on reservoir production performance in the GPSNet model. **(a)** Polymer injection volume. **(b)** Polymer injection concentration. **(c)** Polymer injection rate.

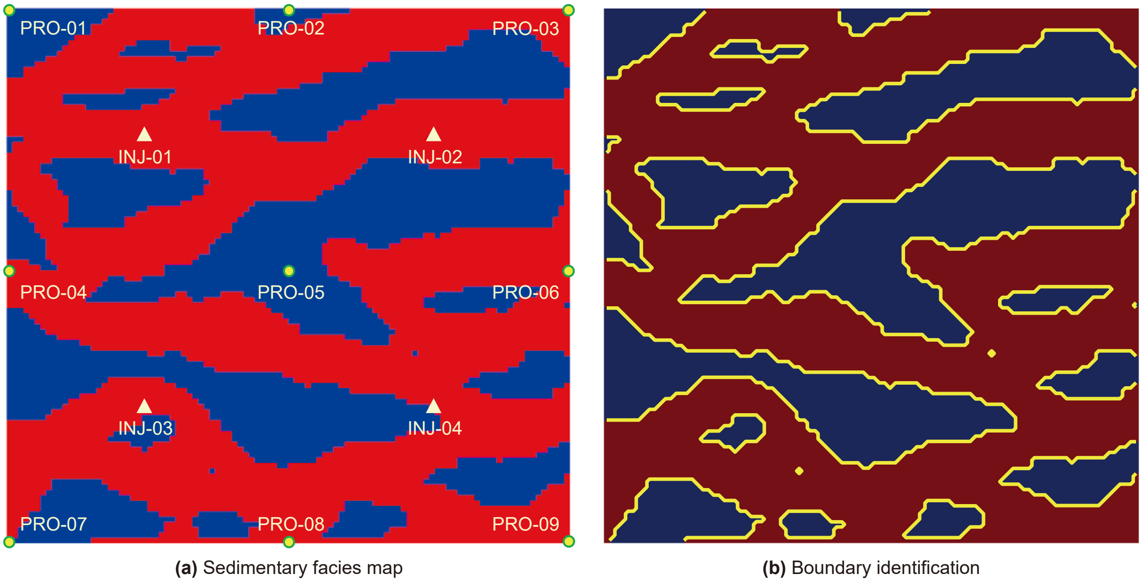

Fig. 13. Sedimentary facies map and boundary identification for Example 2. **(a)** Sedimentary facies map. Red represents high-permeability facies, and blue represents bedrock facies. **(b)** Boundary identification. Yellow curves represent sedimentary facies boundaries.

$$\begin{cases} 0.9 \le \dfrac{\sum_{i=1}^{N_{\mathrm{I}}} q_{\mathrm{wi},i}^{t} + \sum_{k=1}^{N_{\mathrm{PI}}} q_{\mathrm{pi},k}^{t}}{\sum_{j=1}^{N_{\mathrm{P}}} q_{\mathrm{p},j}^{t}} \le 1.1 \\ u^{\mathrm{low}} \le u \le u^{\mathrm{up}} \\ P_{\min} \le P \le P_{\max} \end{cases} \tag{19}$$

Constraint (1) indicates that the total injection-production ratio of the oil field needs to be between 0.9 and 1.1. u^{low} and u^{up}represent the lower and upper bounds of the variable u, which are determined based on the actual production conditions and operational constraints of the oil field. The injection and production rates are restricted within ranges that comply with the capacity of the wells and surface facilities, ensuring that the optimized results remain physically realistic and operationally feasible. $P_{\min}$ and $P_{\max}$ are the lower and upper bounds of the control pressure for the wells. The production optimization problem is solved using the DE Algorithm (Das and Suganthan, 2010) in this study.

3. Experimental results and discussion

This section aims to validate the accuracy of the GPSNet-FC model through three 2D reservoir cases and one real reservoir field, with the computational results from the commercial reservoir simulator Eclipse serving as the reference values for the 2D reservoir models. Specifically, Example 1 aims to verify the correctness of the GPSNet framework in polymer flood simulations and to conduct a sensitivity analysis of various parameters related to polymer flooding. Example 2 seeks to demonstrate that, compared to the GPSNet framework, the GPSNet-FC model can effectively improve the accuracy of history matching and the reliability of predictions in polymer flood scenarios. Example 3 validates the effectiveness of the production optimization method that considers polymer flooding based on the model after history matching in Example 2. Finally, Example 4 is provided to assess the applicability of the model in real reservoir applications.

3.1. Example 1: polymer flooding simulation and sensitivity analysis

The GPSNet-FC method is an improvement based on the GPSNet framework, so we first need to verify that GPSNet can be used in polymer flooding, and polymer-related parameters and mechanisms can be considered in the model. So, this example aims

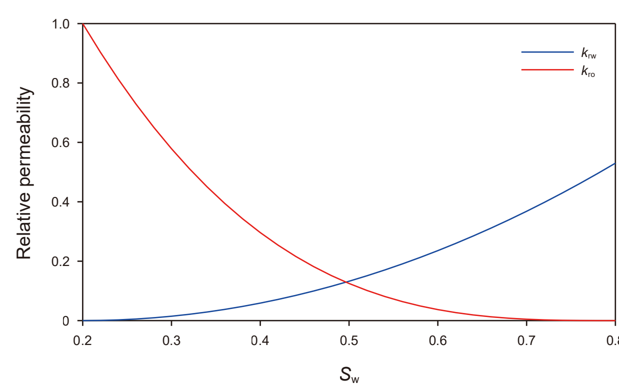

Fig. 14. Relative permeability curve. The blue line represents the water-phase relative permeability, and the red line represents the oil-phase relative permeability.

Table 1
Reservoir and fluid physical properties used in Example 2.

Properties	Value	Properties	Value
Initial reservoir pressure	40 MPa	Oil density	850 kg/m^3
Rock compressibility	2.00e−4 MPa^{-1}	Water density	1000 kg/m^3
Oil compressibility	2.00e−4 MPa^{-1}	Initial oil saturation	0.80
Water compressibility	2.00e−4 MPa^{-1}	Irreducible water saturation	0.20
Oil viscosity	20.00 cp	Residual oil saturation	0.2
Water viscosity	1.20 cp	Wellbore radius	0.2 m

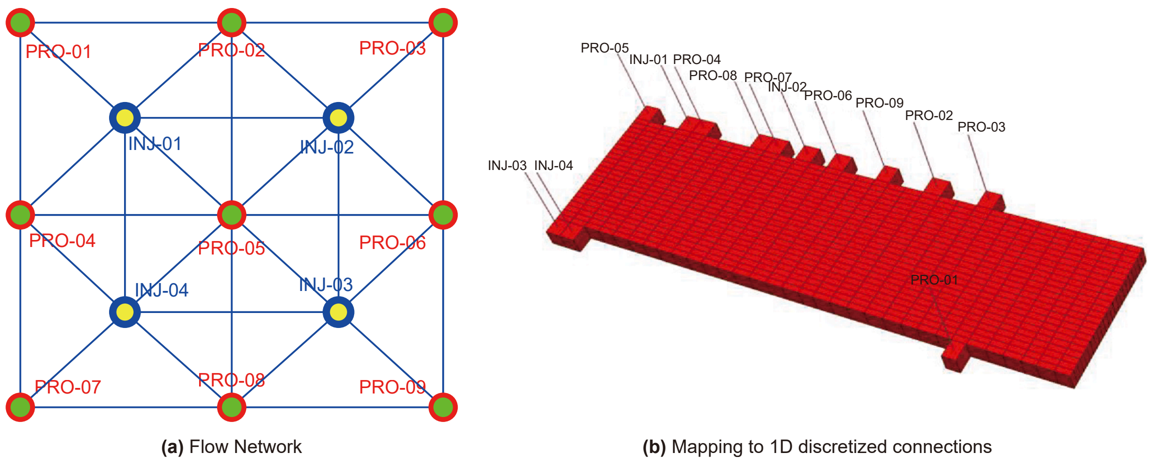

Fig. 15. Model construction in Example 2. **(a)** Flow network. **(b)** Mapping to 1D discretized connections.

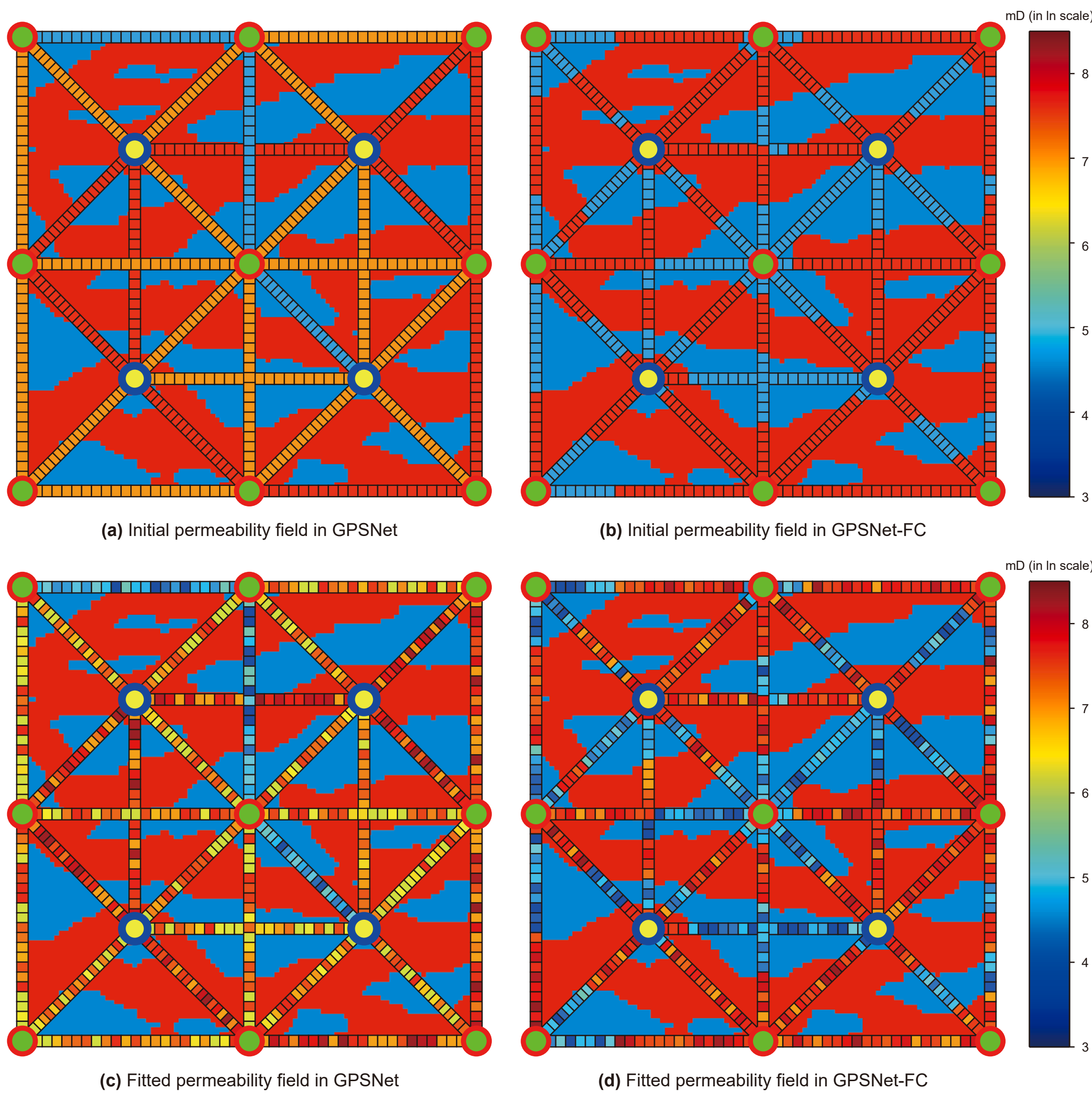

Fig. 16. Comparison of permeability fields before and after history matching. **(a)** Initial permeability field in GPSNet. **(b)** Initial permeability field in GPSNet-FC. **(c)** Fitted permeability field in GPSNet. **(d)** Fitted permeability field in GPSNet-FC. The blue background represents the sedimentary facies field from the Eclipse model. The color within the connecting channels indicates the permeability of grids, with red representing higher and blue representing lower.

to verify the effectiveness of the GPSNet framework, which simplifies a 2D grid into a 1D connection, in simulating polymer flooding. A simple 2D homogeneous reservoir model (with permeability of 100 mD) is considered. The Cartesian grid is shown in Fig. 10(a). The reservoir dimensions are 400 m × 400 m × 2 m, and the number of grids is 10 × 10 × 1. One water injection well is located in the lower-left corner, with an injection rate of 100 m^3/d, and one production well is located in the upper-right corner, with a production rate of 100 m^3/d. Water injection starts from the initial time step, and at day 1500, a polymer solution with a concentration of 0.5 kg/m^3 is injected, with water injection resuming at day 1800. The total injection time is 3600 days, and the production well maintains a constant production rate of 100 m^3/d throughout the process.

Since this case represents a simple homogeneous reservoir with one injector and one producer, the streamline pattern is expected to expand outward from the injector and then converge toward the producer. Therefore, we constructed a spindle-shaped 1D grid model, as illustrated in Fig. 10(b) (Lerlertpakdee et al., 2014), to preserve physical consistency while skipping the history-matching process. Specifically, the total distance between two wells is denoted as L, and the number of grids is N. The grid width is thus $d = L/N$, and the interwell rectangular domain is evenly divided into N segments. The length of the n-th grid cell is calculated as $h_n = N - |2n - (N+1)|d$, and assuming a constant formation thickness H, the volume of the n-th grid cell is given by $V_n = d \times H \times h_n$, as shown in Fig. 10(c). Meanwhile, for comparison, we also present the case without the volume profiles sketched in Fig. 10(b), as shown in Fig. 10(d).

Fig. 11 compares the water-cut results obtained from simulations using the GPSNet and Cartesian grids under two different volume-assignment patterns. The black circles represent the results obtained from the Cartesian grid simulation, the red curve corresponds to the GPSNet simulation with a flow-physics-consistent grid volume distribution, and the blue curve represents the GPSNet simulation with a uniform grid volume distribution. It can be observed that both models show a decreasing water cut, forming a “funnel-shaped” trend after polymer injection on day 1500. The water-cut curve of the GPSNet model that preserves physical and geometric consistency closely matches that of

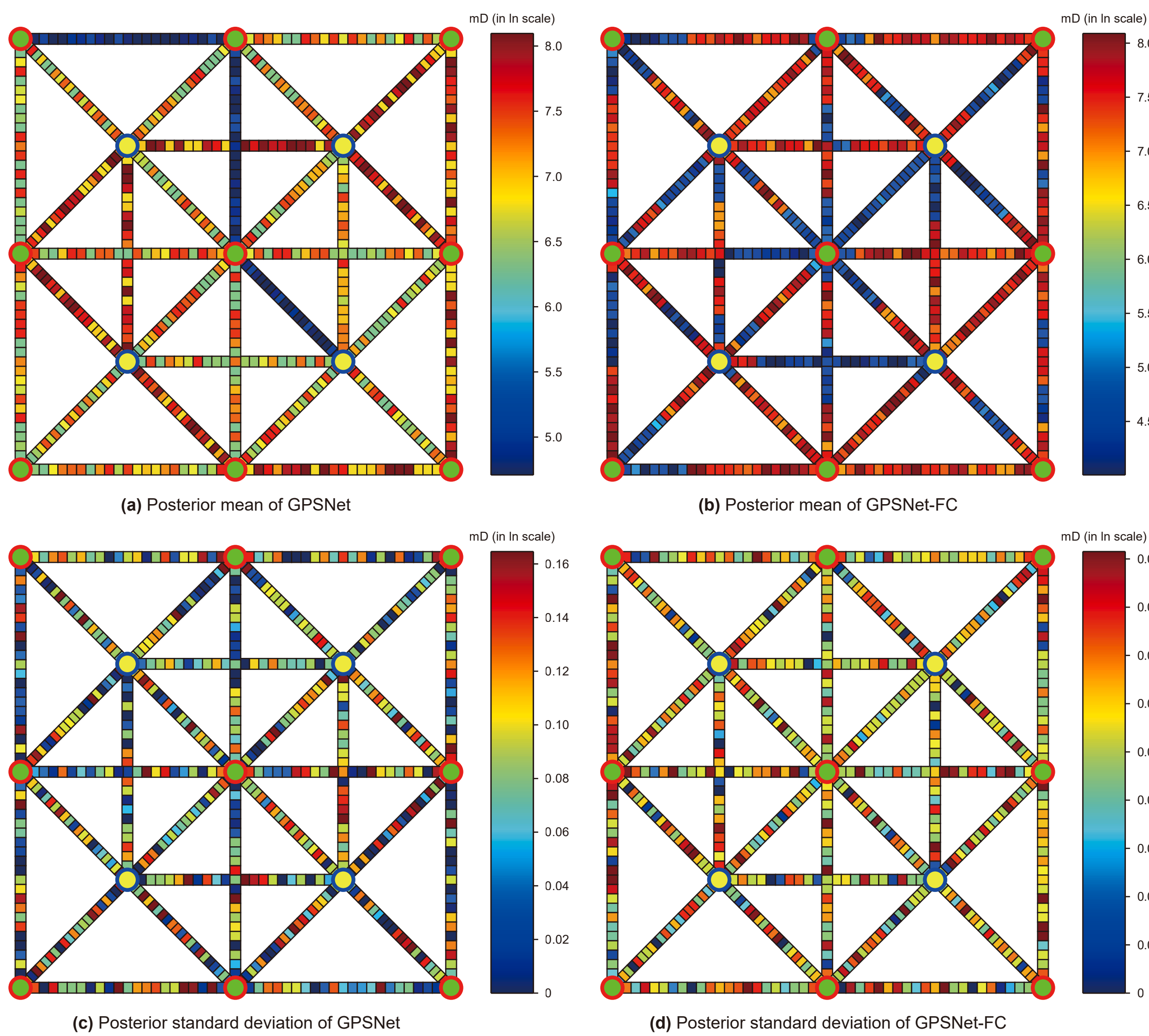

Fig. 17. Mean and standard deviation of posterior permeability distributions after history matching using the GPSNet and GPSNet-FC models. **(a)** Posterior mean of GPSNet. **(b)** Posterior mean of GPSNet-FC. **(c)** Posterior standard deviation of GPSNet. **(d)** Posterior standard deviation of GPSNet-FC.

the Cartesian model, whereas the uniform-grid case exhibits a noticeable deviation. Therefore, it can be concluded that although GPSNet simplifies the two-dimensional Cartesian grid into a one-dimensional finite-difference grid, it still maintains the accuracy of the forward simulation, demonstrating the validity of the GPSNet model for polymer flooding scenarios.

We conducted a sensitivity analysis on the impact of polymer parameters on reservoir production performance. The primary focus was on testing the effects of polymer injection volume, polymer concentration, and polymer injection rate on the degree of reduction in the water cut curve. During the analysis of each parameter's sensitivity, only the parameter under consideration was varied, while all other parameters remained constant. The results are shown in Fig. 12.

In this example, the polymer injection concentration in the sensitivity analysis was varied from 1.2 to 2.0 kg/m^3, which falls within the commonly applied field range of 1.0–2.5 kg/m^3 (Wang et al., 2008). The total injected polymer slug volume was set between 0.2 and 0.6 PV, corresponding to the range used in industrial polymer flooding projects (typically 0.3–0.7 PV) (Wang et al., 2008). The polymer injection rate was designed to be consistent with field injection conditions in order to maintain reservoir pressure and achieve effective mobility control. Accordingly, the injection rate in this study was set between 40 and 120 m^3/d. These parameter settings ensure that the sensitivity analysis closely reflects realistic reservoir operation scenarios and provides practical insights for polymer flooding design.

From the sensitivity analysis, we concluded that, under the condition that other parameters remain the same, the larger the polymer injection volume, the more the water cut curve shifts to the lower-right; the higher the polymer concentration, the deeper the "funnel" of the water cut curve; and the higher the injection rate of the polymer solution, the more the water cut curve shifts to the upper-left. Different combinations of polymer parameters result in different production outcomes, which demonstrates that considering polymer displacement in the GPSNet framework is effective. Therefore, we can use GPSNet-FC based on the GPSNet framework to do further study on polymer flooding optimization.

3.2. Example 2: history matching and prediction for polymer flooding

This example aims to test the fitting and prediction performance of the GPSNet-FC model, which incorporates the sedimentary facies map, compared to the GPSNet framework, in handling reservoirs with distinct sedimentary distribution. Therefore, a two-dimensional channelized reservoir model with fluvial facies deposition is designed. The permeability field consists of a transverse band of high-permeability channels embedded in a low-permeability bedrock facies, as shown in Fig. 13, where the channel facies with a prior permeability (in ln scale) of 7.7 mD and the background facies with a permeability of 4.6 mD. The model dimensions are 400 m $\times$ 400 m $\times$ 2 m, the number of grids is 100 $\times$ 100 $\times$ 1, and the porosity is 0.2. Four injection wells and nine production wells are evenly distributed throughout the reservoir. The relative permeability curves are shown in Fig. 14, and other reservoir properties are listed in Table 1.

We used the full-grid Eclipse model to simulate a total of 3900 days of production history as observation data. Among them, the first 2100 days of water flooding history were used for model

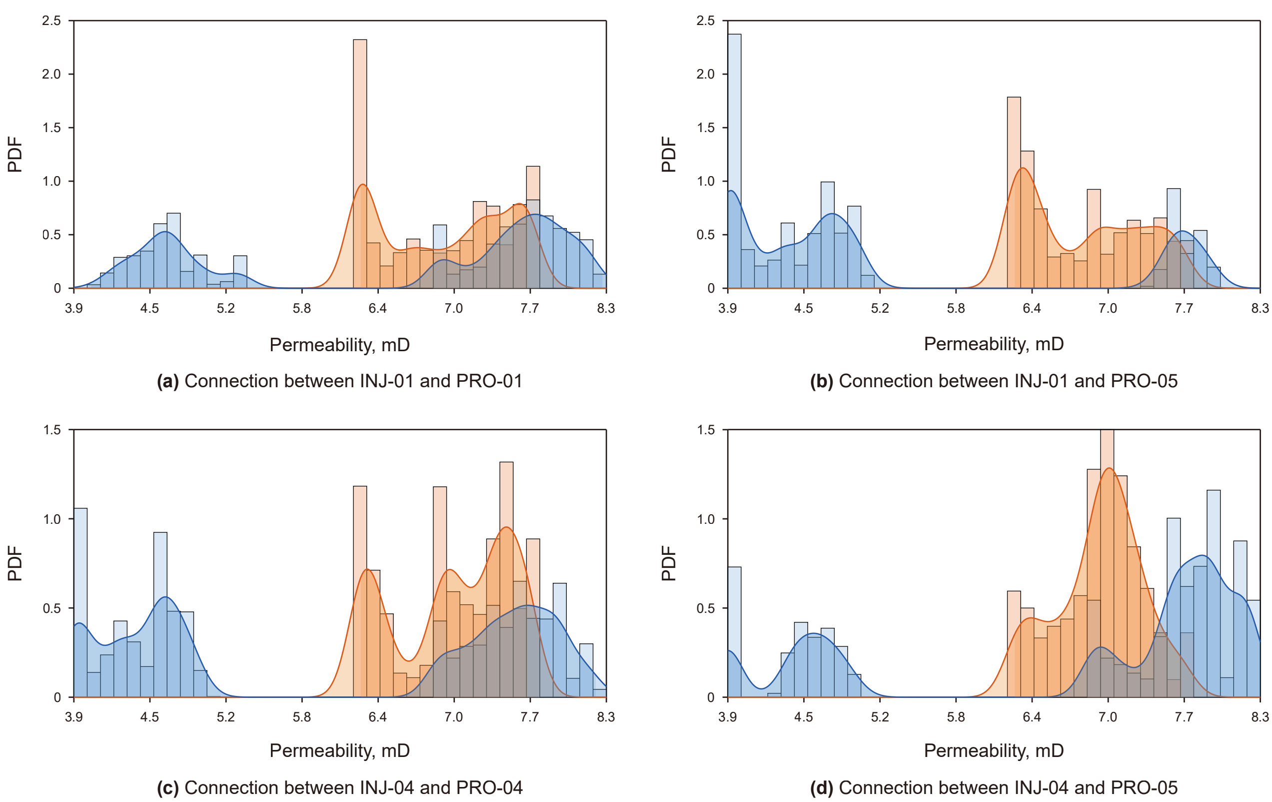

Fig. 18. Probability density distribution of permeability for the inter-well connection. Orange denotes the GPSNet results, and blue denotes the GPSNet-FC results. The histograms represent the sampled permeability distributions from the posterior ensembles, while the smooth curves represent the fitted probability density functions (PDFs). **(a)** Connection between INJ-01 and PRO-01. **(b)** Connection between INJ-01 and PRO-05. **(c)** Connection between INJ-04 and PRO-04. **(d)** Connection between INJ-04 and PRO-05. The permeability is in ln scale.

calibration, and the following 1800 days of production history were used to validate the prediction performance of GPSNet-FC and GPSNet. In the model, the four injection wells started injecting water from the initial time and maintained a constant injection rate of 22.5 m^3/d. Starting from day 2100, a polymer solution with a concentration of 0.5 kg/m^3 was injected, and water injection resumed on day 2400. Nine production wells maintained a constant production rate of 10 m^3/d throughout.

First, we used edge detection and level set methods to identify the phase boundaries of the reservoir model, as shown in Fig. 13(b). The facies boundaries are mostly accurately detected. Based on this, we constructed the GPSNet-FC model by integrating well control and completion information. For comparison, we also constructed the GPSNet model. The difference between the two models does not lie in the model structure; therefore, the flow network models for both are shown in Fig. 15(a). There are 32 connections in the model. The connection mapping diagram is shown in Fig. 15(b), where each connection unit is discretized into 25 grid cells, including 23 connection grid cells and 2 possible well cells at both ends of the connection. The permeability field diagrams for the initialized GPSNet and GPSNet-FC models are shown in Fig. 16(a) and (b), and the grid volumes were initialized uniformly. To facilitate the observation of the relationship between the constructed models and the sedimentary facies, we overlay the

Table 2
FOPT and FWCT errors in the history matching and prediction process of GPSNet and GPSNet-FC in Example 2.

Field, %	FOPT-HM	FWCT-HM	FOPT-Pre	FWCT-Pre
GPSNet-prior	33.59	3.27	142.55	48.24
GPSNet-posterior	2.59	0.82		
GPSNet-FC -prior	43.37	4.18	0.35	2.79
GPSNet-FC -posterior	1.28	0.37		

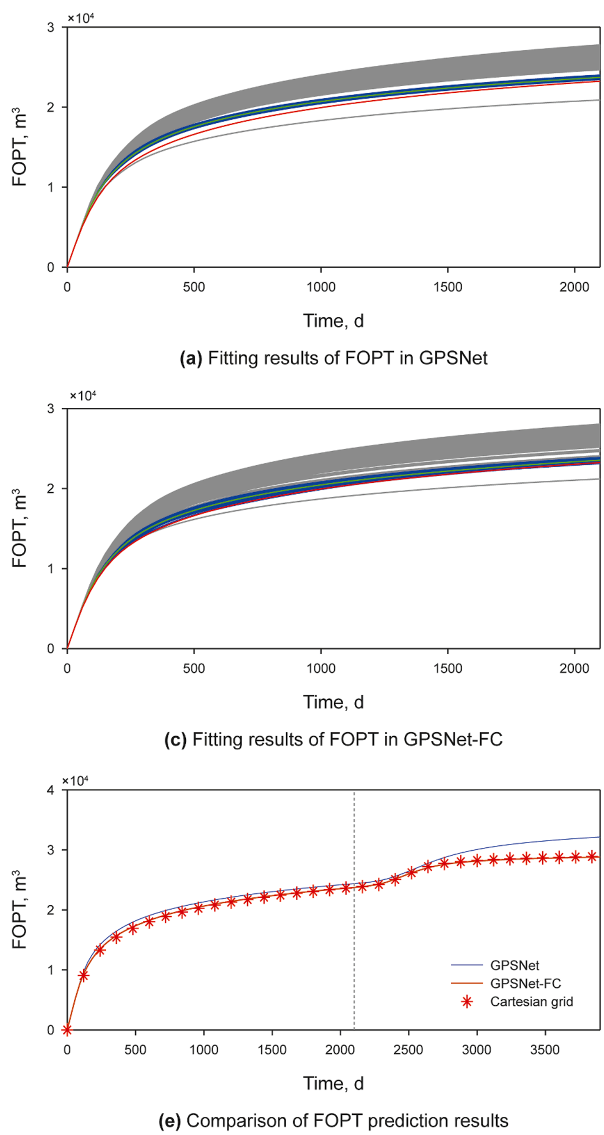

(a) Fitting results of FOPT in GPSNet
(b) Fitting results of FWCT in GPSNet
(c) Fitting results of FOPT in GPSNet-FC
(d) Fitting results of FWCT in GPSNet-FC
(e) Comparison of FOPT prediction results
(f) Comparison of FWCT prediction results

Fig. 19. Fitting and prediction results of cumulative oil production and water cut for the field. **(a)** Fitting results of FOPT in GPSNet. **(b)** Fitting results of FWCT in GPSNet. **(c)** Fitting results of FOPT in GPSNet-FC. **(d)** Fitting results of FWCT in GPSNet-FC. The gray curve cluster represents the prior model results, the blue curve cluster represents the posterior model results, the red curve represents the Eclipse simulation results, and the green curve represents the mean of the posterior results. **(e)** Comparison of FOPT prediction results. **(f)** Comparison of FWCT prediction results. The dashed line divides the time into the history matching stage and the prediction stage. The blue line represents the GPSNet prediction results, the orange line represents the GPSNet-FC prediction results, and the red dots represent the Eclipse simulation results.

flow network connection diagram on top of the permeability field diagram in Fig. 13(a). The red background represents the high-permeability channel facies, and the blue background represents the low-permeability bedrock facies. The color depth of the grid cells in the connections indicates the permeability value, with red indicating higher permeability and blue indicating lower permeability. During model initialization, the grid parameters in the GPSNet model are assigned based on the average values of the properties at the two connected well points. So, all grid cells within the same connection share identical properties, as illustrated in Fig. 16(a). In contrast, GPSNet-FC captures more detailed depositional facies characteristics during grid property assignment, providing a stronger foundation for its more reliable predictive capability.

During the history matching process, we used the well oil production rate (WOPR) as the observation data, with the fitting parameters being the permeability and grid volume between each grid. The population size for the history matching was set to 250, with 15 loop iterations. The prior permeability of each facies was sampled within ± 0.5 mD around the initial permeability (in ln) of that facies, while the prior grid volumes were sampled within the range of [0.5, 2] times their initial values (Wang et al., 2022). The optimal model obtained after history matching for GPSNet and GPSNet-FC is shown in Fig. 16(c) and (d), respectively, with a consistent color scale applied to both the background and the network cell values. Similarly, the color intensity represents the magnitude of the permeability values. The posterior grid volumes obtained after history matching are no longer uniform, but their variation is difficult to visualize in the schematic plots due to geometric simplification and scale limitations. To minimize the objective function during history matching, GPSNet, which lacks depositional facies constraints, searches for the optimal solution across the entire parameter space. As a result, its permeability distribution exhibits a disordered and random pattern, where low-permeability regions may display high values and vice versa. In contrast, the history-matched results of GPSNet-FC, constrained by the depositional facies map, demonstrate better consistency with geological understanding. Therefore, in terms of geological consistency, the overall credibility of the GPSNet-FC model after fitting is higher than that of the GPSNet model.

To further quantify how facies constraints reduce the non-uniqueness of history matching, we performed statistical analyses on the posterior permeability fields obtained from 250 ensemble realizations. Fig. 17 presents the mean and standard

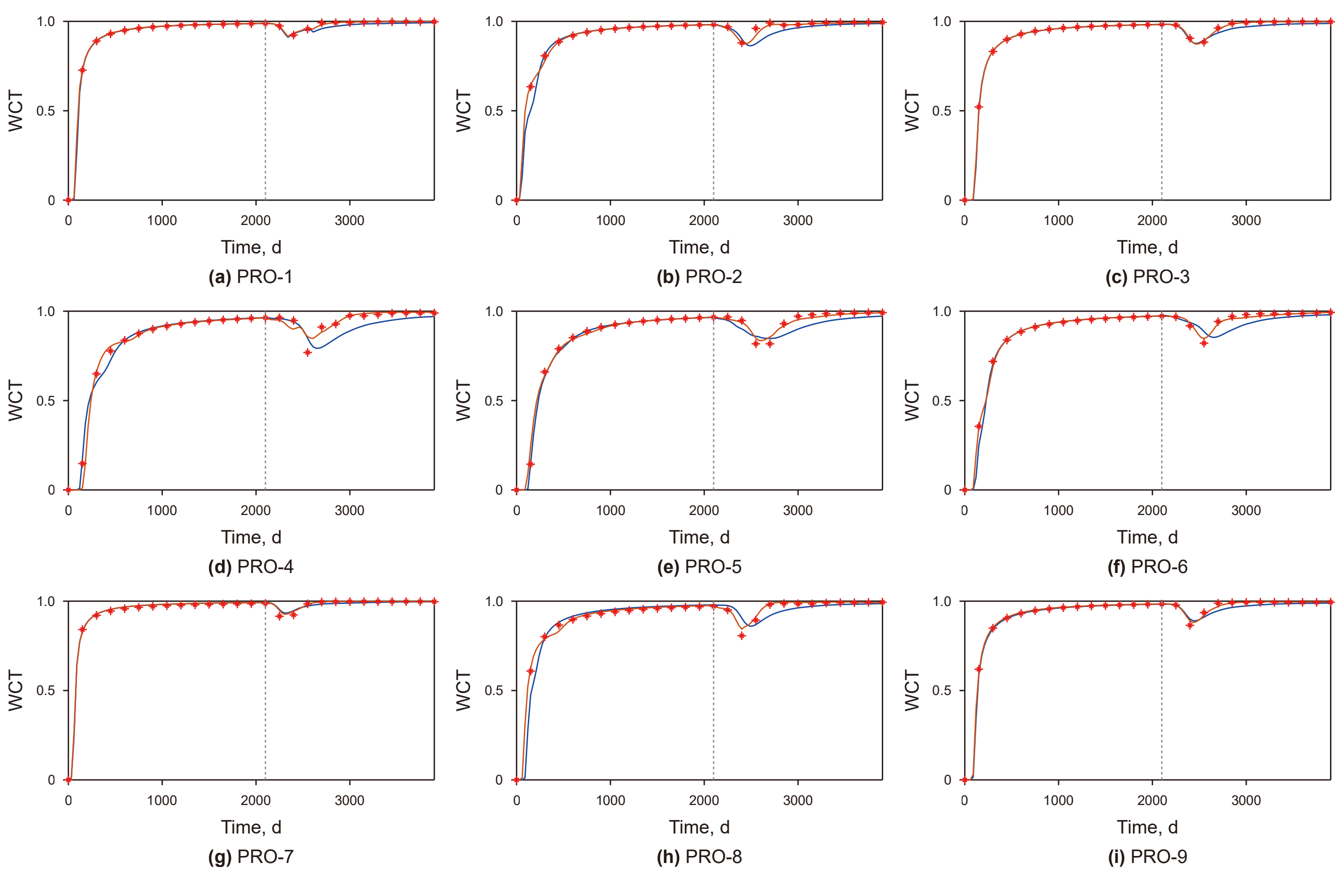

Fig. 20. Prediction results of water cuts for each well of Example 2. The dashed line divides the time into the history matching stage and the prediction stage. The blue line represents the GPSNet prediction results, the orange line represents the GPSNet-FC prediction results, and the red dots represent the Cartesian grid simulation results.

Table 3
WCT errors in the prediction process of GPSNet and GPSNet-FC in Example 2.

Prediction, %	PRO-1	PRO-2	PRO-3	PRO-4	PRO-5	PRO-6	PRO-7	PRO-8	PRO-9	All
GPSNet	38.77	129.57	19.14	111.10	53.41	80.71	23.27	54.69	34.30	59.52
GPSNet-FC	6.09	17.49	0.92	21.34	8.53	6.13	14.00	7.15	8.81	9.43

deviation of the posterior permeability distributions for both GPSNet and GPSNet-FC models. When compared with the depositional facies map, it can be observed that GPSNet-FC yields lower permeability means in the bedrock regions and higher values within the high-permeability channel zones, which is more consistent with geological cognition. Conversely, GPSNet produces a nearly uniform and structureless mean distribution, failing to distinguish between high and low-permeability facies. Moreover, the standard deviation of GPSNet-FC (Fig. 17(b)) is notably smaller than that of GPSNet (Fig. 17(d)), indicating that the variability of grid permeability is significantly reduced under the facies constraint. This result confirms that the geological regularization imposed by the facies map effectively narrows the uncertainty range and mitigates the non-uniqueness of history matching.

In addition, the probability density distributions of permeability were analyzed for several inter-well connections, including INJ-01 and PRO-01, INJ-01 and PRO-05, INJ-04 and PRO-04, and INJ-04 and PRO-04, as shown in Fig. 18. The horizontal axis denotes the logarithmic permeability (in ln), while the vertical axis represents the probability density. The yellow histograms and curves correspond to the GPSNet model, and the blue ones correspond to GPSNet-FC. It can be observed that the GPSNet results exhibit a unimodal distribution concentrated below $K = 7.7$ mD (in ln), whereas GPSNet-FC shows a clear bimodal distribution, corresponding respectively to the low-permeability bedrock and high-permeability channel facies. This bimodal behavior aligns closely with the geological understanding of the sedimentary system and further demonstrates that incorporating facies constraints not only enhances geological consistency but also effectively reduces parameter uncertainty and solution non-uniqueness during history matching.

The field oil production total (FOPT) and field water cut total (FWCT) fitting results for both GPSNet and GPSNet-FC models are shown in Fig. 19(a)–(d). In these figures, the gray curve clusters represent the prior model simulation results, the blue curve clusters represent the posterior model simulation results, the red curve represents the full-grid Eclipse simulation results, and the green curve represents the posterior model mean. The early increase in water cut at the beginning of production is mainly attributed to the small size of the reservoir model and the direct connectivity between the injector and producer through the high-permeability channel. In this configuration, the injected water quickly travels along the high-permeability pathway and reaches the production well, resulting in an immediate rise in water cut. This design was intentional, as it allows the reservoir to rapidly reach a high water-cut level of approximately 90%, which facilitates the subsequent analysis and optimization of polymer flooding. Columns 1–2 of Table 2 show the errors between the prior and posterior models of both GPSNet and GPSNet-FC compared to the FOPT and FWCT values calculated by full-grid Eclipse model. The Normalized Mean Squared Error (NMSE), calculated using Eq. (20), is used to measure the difference between the models. We found that, compared to the prior ensemble, the posterior error for FOPT in both models decreased to within 3%, and the posterior error for FWCT decreased to within 1%. This shows that, through the history matching process, both models can adjust their parameters to align the production dynamics with the actual historical data.

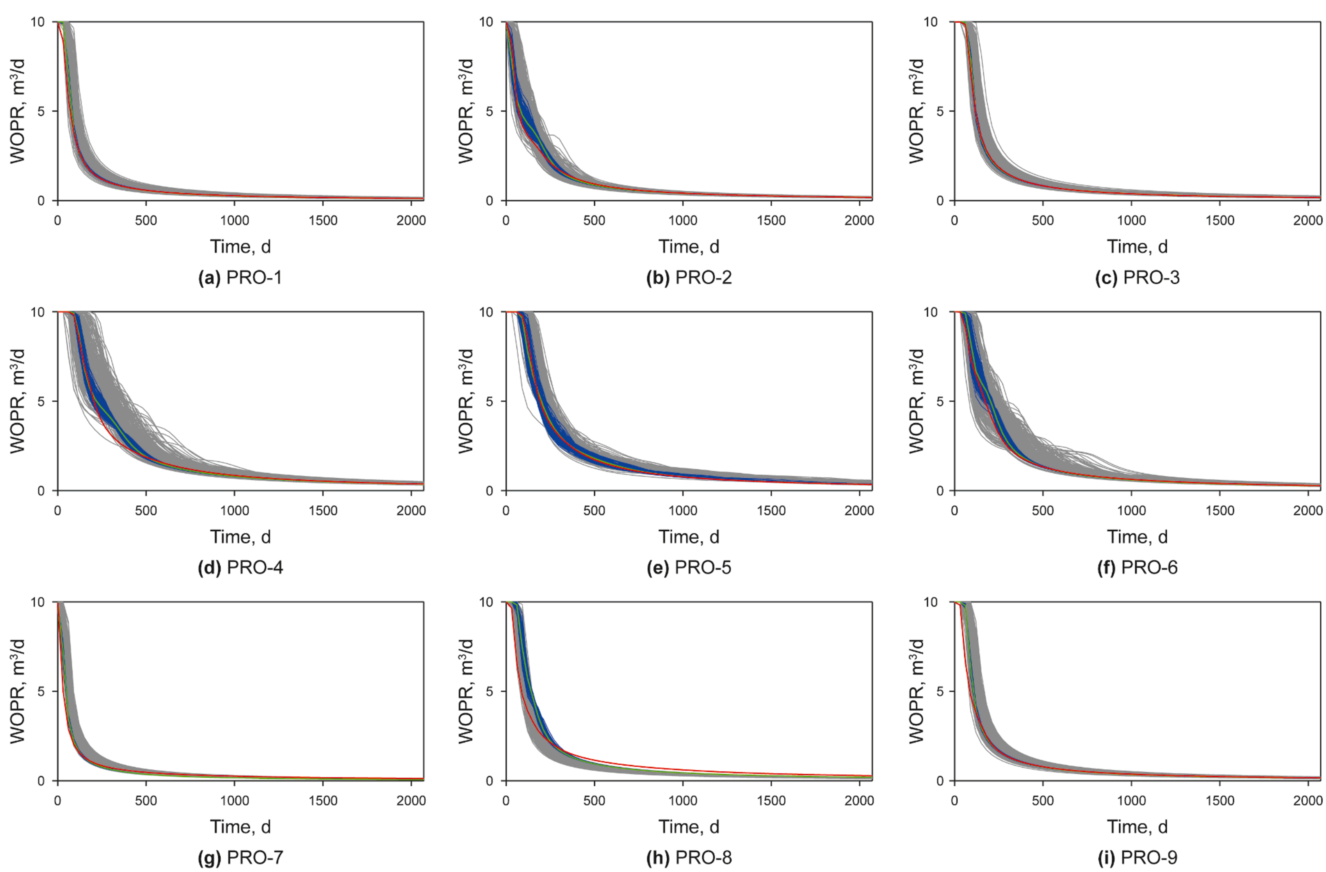

Fig. 21. History matching results of oil production rates for each well in the GPSNet framework of Example 2. The gray curve cluster represents the prior model results, the blue curve cluster represents the posterior model results, the red curve represents the Eclipse simulation results, and the green curve represents the mean of the posterior results.

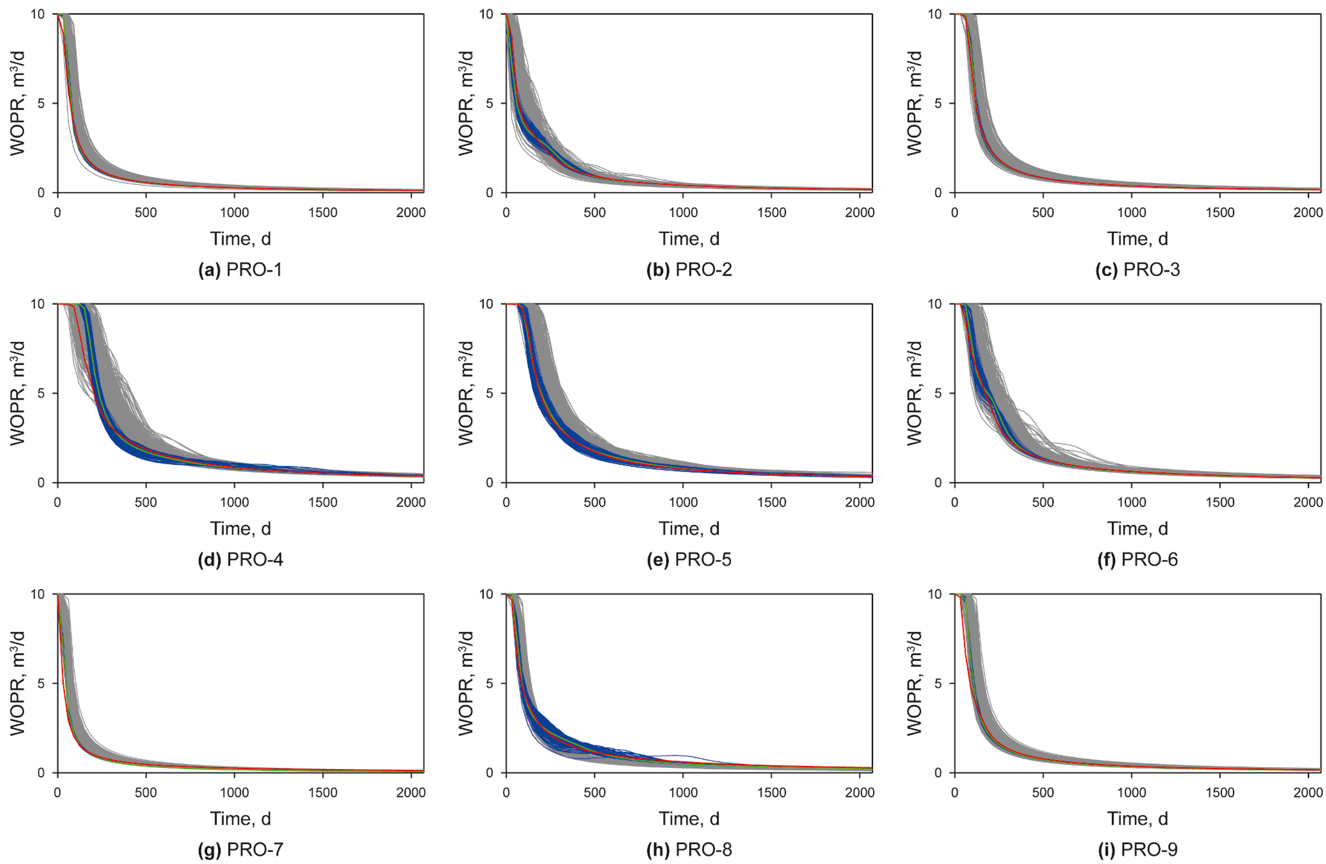

Fig. 22. History matching results of oil production rates for each well in the GPSNet-FC model of Example 2. The gray curve cluster represents the prior model results, the blue curve cluster represents the posterior model results, the red curve represents the Eclipse simulation results, and the green curve represents the mean of the posterior results.

Table 4
WOPR errors in the history matching process of GPSNet and GPSNet-FC in Example 2.

WOPR-HM, %	PRO-1	PRO-2	PRO-3	PRO-4	PRO-5	PRO-6	PRO-7	PRO-8	PRO-9	All
GPSNet-prior	10.14	7.65	3.87	9.11	3.49	5.79	26.96	7.97	12.90	7.81
GPSNet-posterior	1.49	1.59	0.14	1.06	0.48	1.28	4.41	7.62	5.14	2.32
GPSNet-FC-prior	10.00	6.66	4.12	11.20	8.33	7.22	27.15	7.91	13.15	9.09
GPSNet-FC-posterior	1.14	1.63	0.23	4.17	0.41	0.93	3.86	1.12	4.87	1.84

Table 5
WOPR errors in the posterior models of GPSNet and GPSNet-FC during five history matching iterations. The bolded are the models with the smallest error.

WOPR-HM, %	HM_1	HM_2	HM_3	HM_4	HM_5
GPSNet-posterior	2.74	**2.58**	3.01	2.63	2.86
GPSNet-FC -posterior	2.32	2.19	**2.04**	2.10	2.27

$$\mathrm{NMSE} = \frac{\sum_{i=1}^{N}\sum_{j=1}^{M}\left(y_{i,j} - y_{\mathrm{ref},j}\right)^2}{M\sum_{j=1}^{M}\left(y_{\mathrm{ref},j} - \overline{y}_{\mathrm{ref},j}\right)^2} \tag{20}$$

where N is the number of curves, M is the number of points in each curve, y is the computed data, y_{ref} is the reference data, and $\overline{y}_{\mathrm{ref}}$ is the mean of the reference data.

Subsequently, we evaluate the prediction performance of the fitted models in the polymer flooding problem. Starting from day 2100, a polymer solution with a concentration of 0.5 kg/m^3 is injected, and water injection is resumed on day 2400. The prediction results for FOPT and FWCT are shown in Fig. 19(e) and (f). The dashed line indicates the historical stage on the left, and the prediction stage on the right. The red dots represent the results from the Cartesian grid, the blue curve shows the predictions from the GPSNet, and the orange curve shows the predictions from the GPSNet-FC model. Specific error data is shown in columns 3–4 of Table 2. Clearly, the GPSNet-FC model, which incorporates sedimentary facies modeling, significantly reduces the errors during the prediction stage. The water-cut prediction results are shown in Fig. 20, which correspond to the predictions obtained from the best model after history matching, while the prediction errors of WCT, which serves as the observation data in the history-matching process, are provided in Table 3. Both models show relatively low prediction accuracy for PRO-04, but overall, the GPSNet-FC model reduces well prediction errors by two-thirds compared to GPSNet, and the error for the overall field performance (FOPT and FWCT) decreases by about one order of magnitude, demonstrating the reliability of the GPSNet-FC model in polymer flooding scenarios.

In order to show that the superior performance of GPSNet-FC in prediction compared with GPSNet is not due to the difference in the randomness of history matching, while the GPSNet-FC model provides a more accurate representation of the underlying reservoir behavior. We have made a detailed presentation of the history matching process as follows. Figs. 21 and 22 show the history matching results for the nine production wells in both models. In the prior model, there was significant uncertainty, but after multiple iterations, the uncertainty range in the posterior model noticeably decreased. Most of the wells match the observed data, achieving a good history matching process. Table 4 presents the concrete fitting errors. Similar to the conclusions drawn from the field performance, GPSNet slightly underperforms compared to GPSNet-FC in terms of fitting accuracy. However, after fitting, the errors for both models were reduced to below 3%, indicating that the fitted models have sufficient accuracy to represent the subsurface reservoir conditions.

To reduce the randomness in the history matching process, we repeated the history matching process five times for both models. Using WOPR error as the performance metric, the results from the five fitting runs are shown in Table 5. The model with the lowest error from each set of iterations was selected as the final prediction model. From Table 5, we can see that GPSNet-FC consistently has lower errors than GPSNet, suggesting that the parameter search space based on sedimentary facies makes it easier to find suitable solutions, and the parameter inversion results after multiple iterations are more accurate.

3.3. Example 3: production optimization in polymer flooding

In this example, we aim to verify the polymer flooding optimization effect of the GPSNet-FC model. Therefore, we directly use the sedimentary facies model fitted in Example 2 as the base model for the subsequent optimization process. During the optimization, we performed 12 control time steps, with each control step being 180 days, for a total development period of 2160 days. The optimization variables include the production rate, water injection rate, and polymer injection concentration for each well. To ensure that the system of each well does not change drastically before and after optimization, the search space for the production rate and water injection rate is set to 0.8 to 1.2 times the initial injection-production system, and the polymer concentration is set between 0 and 2.5 kg/m^3, with polymer injection only occurring during the first four-time steps, and water injection occurring subsequently. For comparison, we maintained a consistent total polymer injection volume, using a polymer solution with a concentration of 1.5810 kg/m^3, injected uniformly into the formation at a rate of 22.5 m^3/d. Meanwhile, we also performed a comparative optimization directly using the Cartesian grid (i.e., the reservoir model that generates the red curve in Fig. 21, applying the same optimization algorithm and constraints as used in GPSNet-FC. Similarly, to maintain the overall injection-production

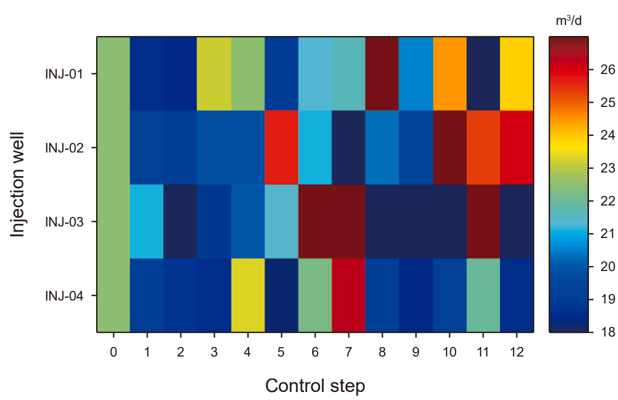

(a) Injection rate optimization results

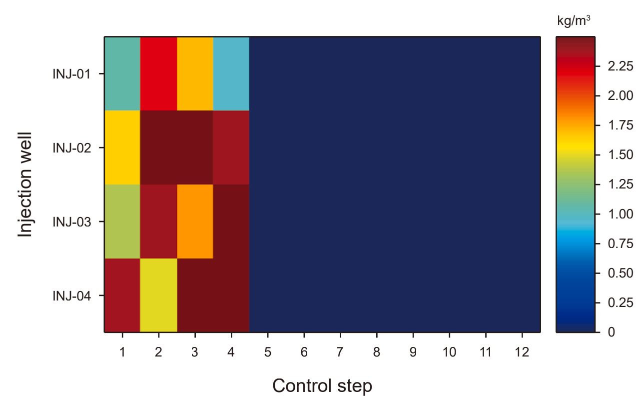

(b) Polymer concentration optimization results

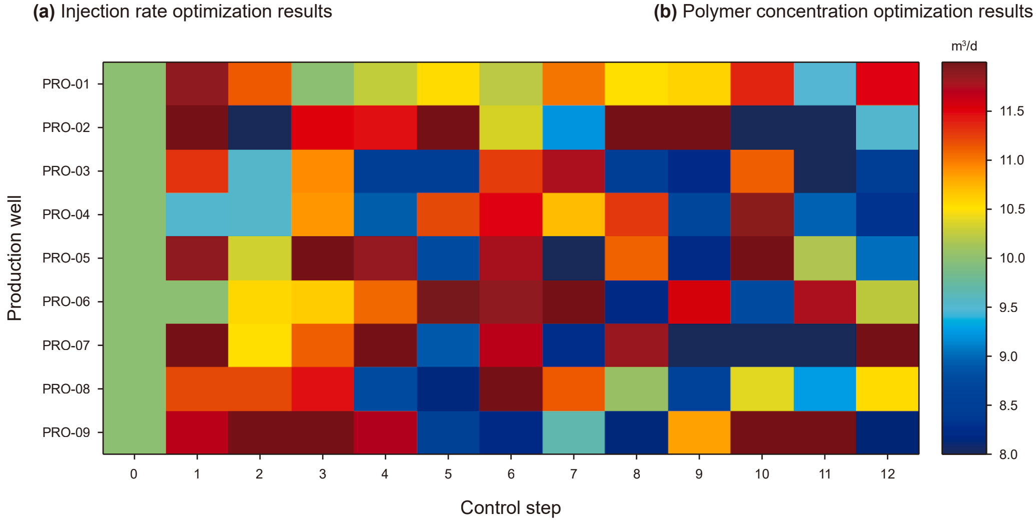

(c) Production rate optimization results

Fig. 23. Optimization results of the well scheme using GPSNet-FC in Example 3. **(a)** Injection rate optimization results. **(b)** Polymer concentration optimization results. **(c)** Production rate optimization results. The vertical axis represents the optimized wells, and the horizontal axis represents the optimized time steps. Each colored block shows the magnitude of the optimization result, with red indicating larger values and blue indicating smaller values.

balance for the field, the injection-production ratio is set between 0.9 and 1.1. The crude oil price is set to 494.49 USD/m^3, the water injection cost is 6.18 USD/m^3, the wastewater treatment cost is 4.63 USD/m^3, and the polymer injection cost is 2527.2 USD/t (Tariq et al., 2018). The population size is 100, and the total number of iterations is 2000. In the differential evolution algorithm, the mutation operator and crossover operator are set to 0.4 and 0.6, respectively, to ensure diversity in the search space.

Fig. 23 shows the optimization results of the well scheme using GPSNet-FC. The vertical axis represents the optimized wells, while the horizontal axis represents the optimized control steps. The “0” means the production scheme at the final time step of the history matching process. This production scheme will be maintained for 12 control steps as the benchmark for comparing the optimization results. Each row represents the optimization results for that well across the 12 optimization control steps, with each colored block representing the magnitude of the optimization result. The color is red for larger values and blue for smaller values. From the figure, it can be observed that the search results of the differential evolution algorithm are irregular. To achieve higher NPV, a well may either increase or decrease its liquid production during its development. This disordered search is something that field operators cannot manually predict, which is a significant advantage of combining intelligent algorithms with oil field development. Fig. 24 shows the optimization results of the well scheme using Cartesian grid. Overall, the optimization results obtained from GPSNet-FC and the Cartesian grid show a certain degree of similarity. In terms of polymer concentration optimization, both models indicate that the polymer concentration injected from INJ-01 is lower than that of the other three injectors. This is likely because INJ-01 has stronger connectivity with the surrounding producers (as shown in Fig. 13(a)), and therefore a lower polymer concentration is sufficient to achieve an efficient displacement effect. For the injection rate optimization, similar patterns can also be observed: the injection rate of INJ-01 increases significantly in the later optimization stages; INJ-02 shows two periods of strong injection (around the 5th–6th and 10th–12th optimization steps); and INJ-04 has a higher injection rate in the early stages. In addition, the final-stage water injection rate in the GPSNet-FC optimization is lower than that obtained from the Cartesian grid, indicating that sufficient reservoir energy has been established through earlier injection. Consequently, the GPSNet-FC model tends to reduce water injection in the later stages to reduce the costs and achieve a higher NPV. These partial similarities suggest that although GPSNet-FC and the Cartesian grid differ in spatial resolution, both models identify similar operational trends when optimizing for maximum NPV.

Fig. 26 presents the curves of cumulative oil production and water cut over development time for several scenarios. The gray curve divides the entire period into the fitting stage and the optimization stage. The black curve represents the water flooding prediction, the blue curve represents the polymer flooding

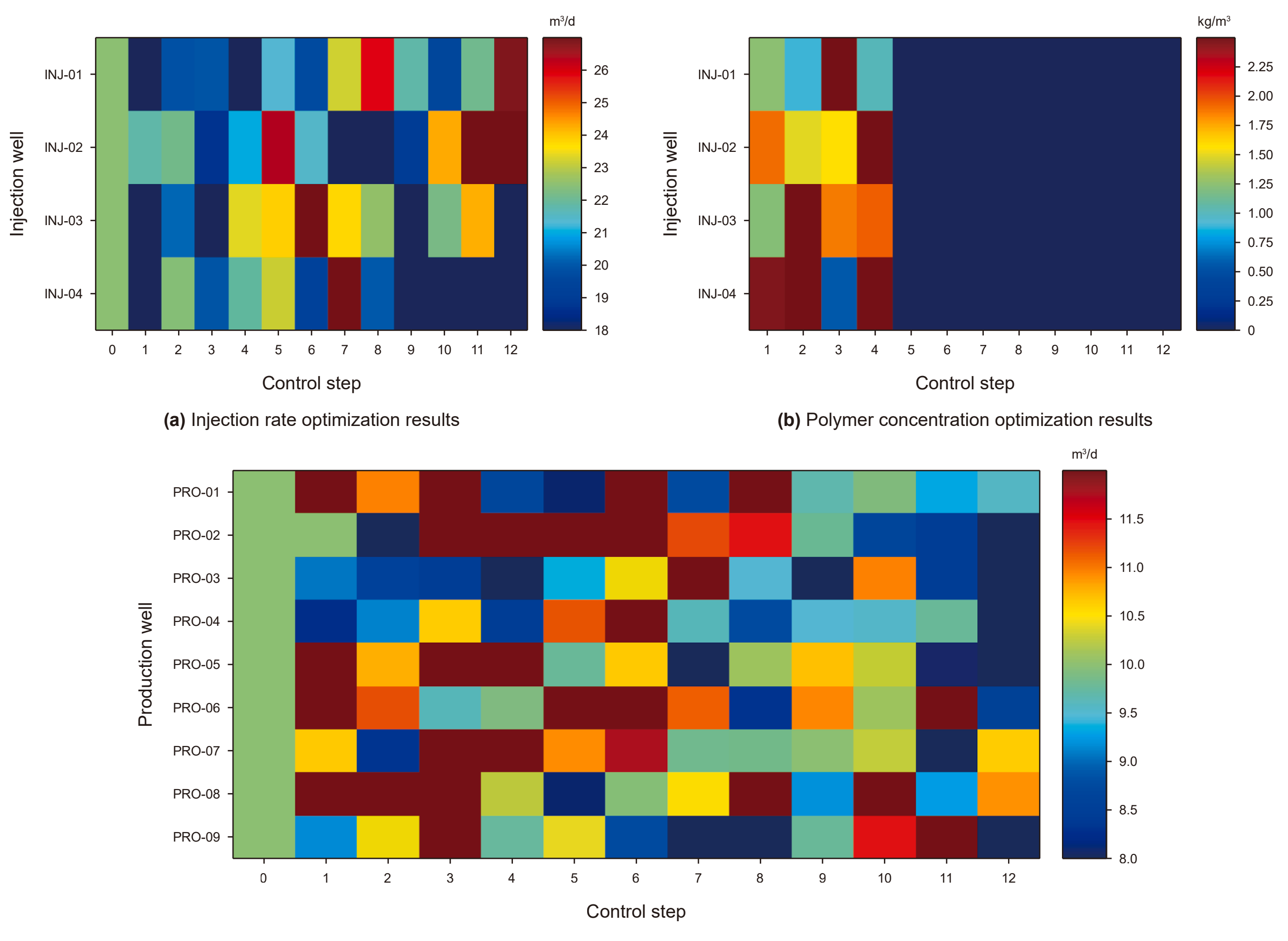

Fig. 24. Optimization results of the well scheme using Eclipse in Example 3. **(a)** Injection rate optimization results. **(b)** Polymer concentration optimization results. **(c)** Production rate optimization results.

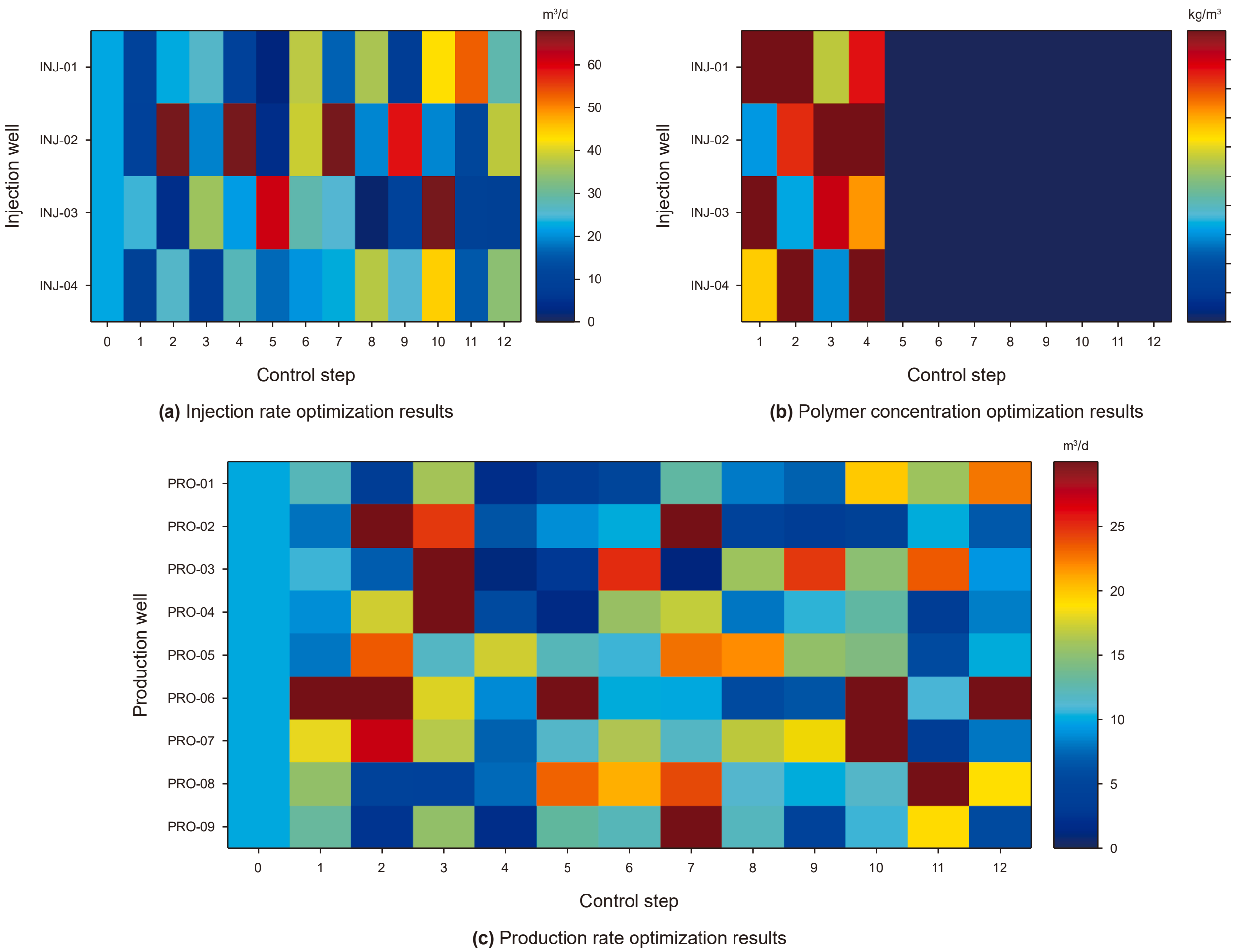

Fig. 25. Optimization results of the well scheme using GPSNet-FC in Example 3 within a larger optimization range. **(a)** Injection rate optimization results. **(b)** Polymer concentration optimization results. **(c)** Production rate optimization results.

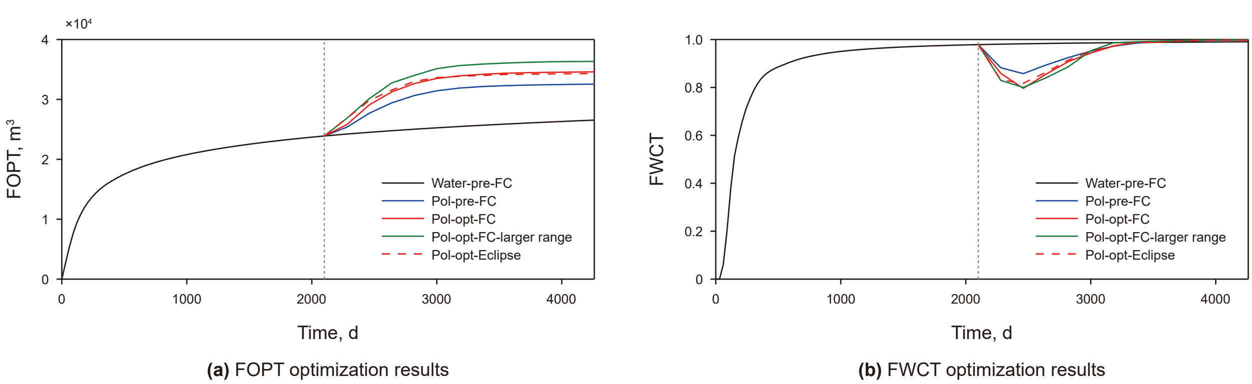

Fig. 26. Field production optimization results. **(a)** FOPT optimization results. **(b)** FWCT optimization results. The gray curve divides the entire period into the fitting stage and the optimization stage. The black curve represents the water flooding prediction, the blue curve represents the polymer flooding prediction, the red solid line represents the polymer flooding optimization result from GPSNet-FC, the green curve represents the optimization result obtained by GPSNet-FC within a much broader parameter search range, and the red dashed line represents the polymer flooding optimization result from Eclipse.

prediction, the red solid line represents the polymer flooding optimization result from GPSNet-FC, and the red dashed line represents the polymer flooding optimization result from Eclipse. Compared to the direct prediction of polymer flooding (blue curve), the GPSNet-FC increased the cumulative oil production by 23.78%, achieving results comparable to those from Eclipse, demonstrating significant optimization effectiveness.

In practical field operations, control actions on injection and production rates are constrained by real engineering and operational considerations (Hoffmann et al., 2019). Large, abrupt changes in well rates can cause frequent equipment start–stop cycles, surface facility pressure fluctuations, and stress on pumps and piping systems, which could compromise operational stability and facility integrity. These considerations motivate the use of

Table 6
Comparison of prediction and optimization results in Example 3.

Model	GPSNet-FC	GPSNet-FC	GPSNet-FC	GPSNet-FC	Eclipse
Strategy	Prediction	Prediction	Optimization	Opt-larger range	Optimization
Injected solution	Water	Polymer	Polymer	Polymer	Polymer
FOPT, 10^4 m^3	2.654	3.254	3.460	3.634	3.432
Min water cut, %	0.978	0.858	0.796	0.805	0.817
NPV, 10^6 USD	0.469	2.600	3.200	3.682	3.105
Time cost	2.21 s	2.21 s	1.28 h	1.29 h	6.65 h

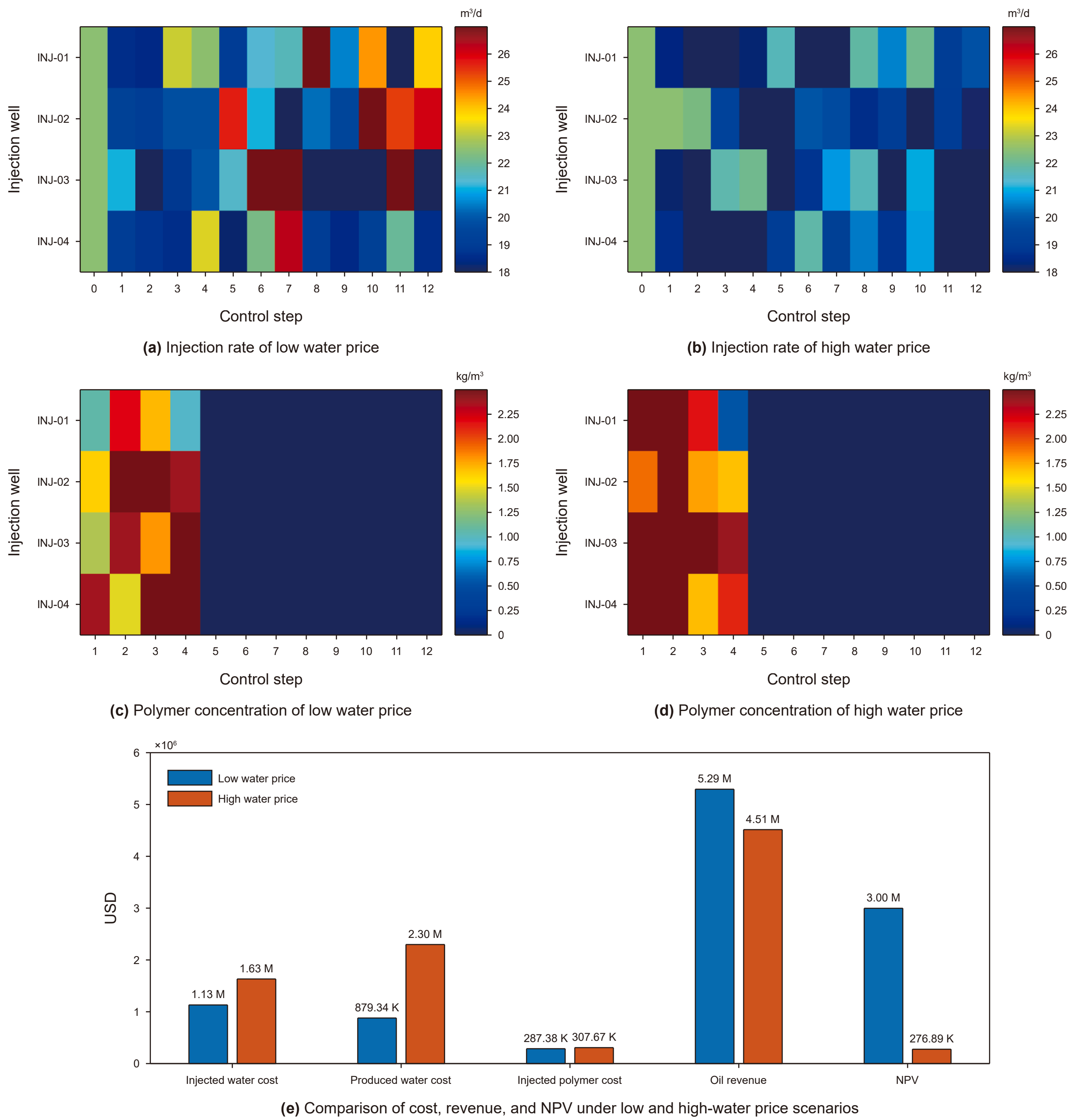

Fig. 27. Comparison of optimization results under low and high oil price scenarios. (**a**) Injection rate of low water price. (**b**) Injection rate of high water price. (**c**) Polymer concentration of low water price. (**d**) Polymer concentration of high water price. The vertical axis represents the optimized wells, and the horizontal axis represents the optimized time steps. Each colored block shows the magnitude of the optimization result, with red indicating larger values and blue indicating smaller values. (**e**) Comparison of cost, revenue, and NPV under low and high-water price scenarios.

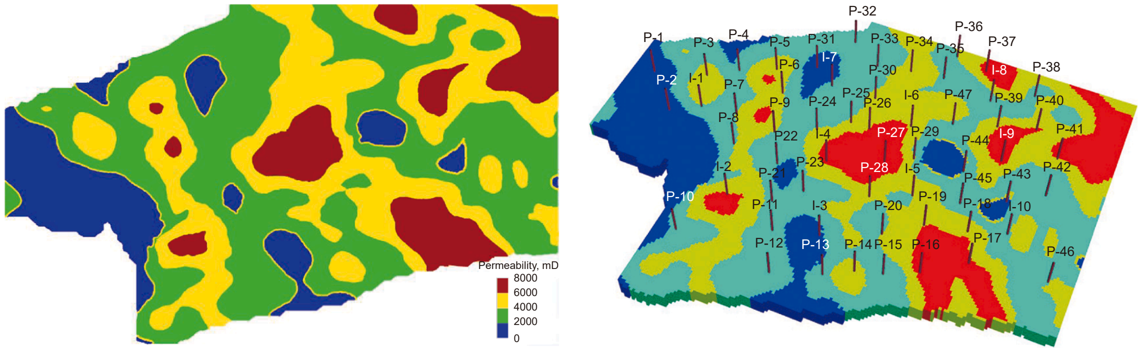

(a) Sedimentary facies boundary identification **(b)** Sedimentary facies boundary identification

Fig. 28. Sedimentary facies boundary identification and Cartesian grid model construction for Example 4. **(a)** Sedimentary facies boundary identification. The four colors represent four different depositional facies. The light yellow curves represent sedimentary facies boundaries. **(b)** Full-grid Eclipse model.

Table 7
Reservoir and fluid physical properties used in Example 4.

Properties	Value	Properties	Value
Rock compressibility	1.50e−4 MPa^{-1}	Oil density	914 kg/m^3
Oil compressibility	2.20e−3 MPa^{-1}	Water density	1000 kg/m^3
Water compressibility	2.20e−3 MPa^{-1}	Residual oil saturation	0.247
Oil viscosity	12.59 cp	Irreducible water saturation	0.204
Water viscosity	1.00 cp	Datum depth	4000 m

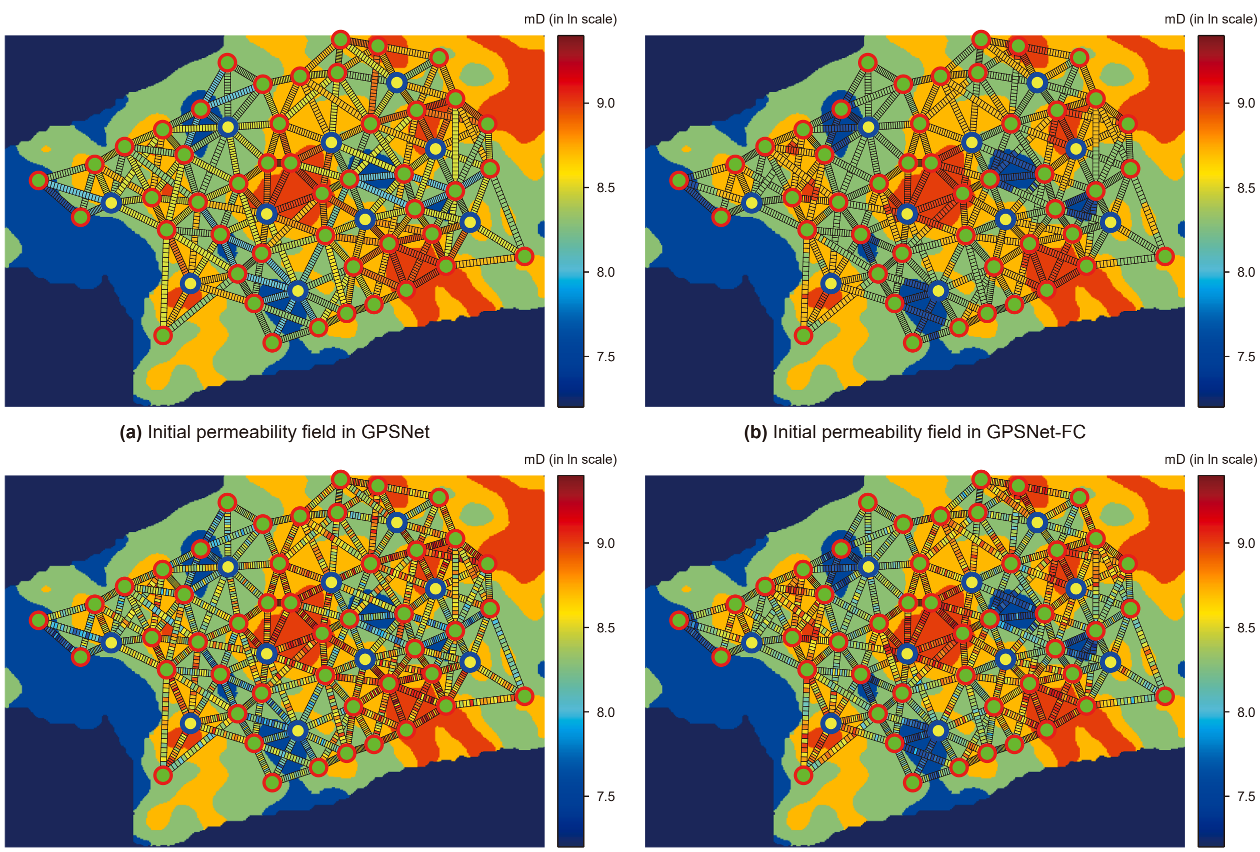

(a) Initial permeability field in GPSNet **(b)** Initial permeability field in GPSNet-FC

(c) Fitted permeability field in GPSNet **(d)** Fitted permeability field in GPSNet-FC

Fig. 29. Initial and fitted permeability field distributions of the GPSNet and GPSNet-FC models. The background represents the depositional facies, while the overlaid grids indicate the flow-network permeability values. Both maps share the same color scale. And the prior ensemble was generated using this initial permeability field as the mean and a standard deviation of 0.4 mD (in ln). **(a)** Initial permeability field in GPSNet. **(b)** Initial permeability field in GPSNet-FC. **(c)** Fitted permeability field in GPSNet. **(d)** Fitted permeability field in GPSNet-FC.

moderate rate adjustment bounds (i.e., 0.8 to 1.2 times the initial injection-production system) to represent typical operational conditions. In addition, we also conducted an additional optimization experiment using the GPSNet-FC model with a significantly expanded control range. As shown in Fig. 25, the upper and lower bounds of both injection and production rates are

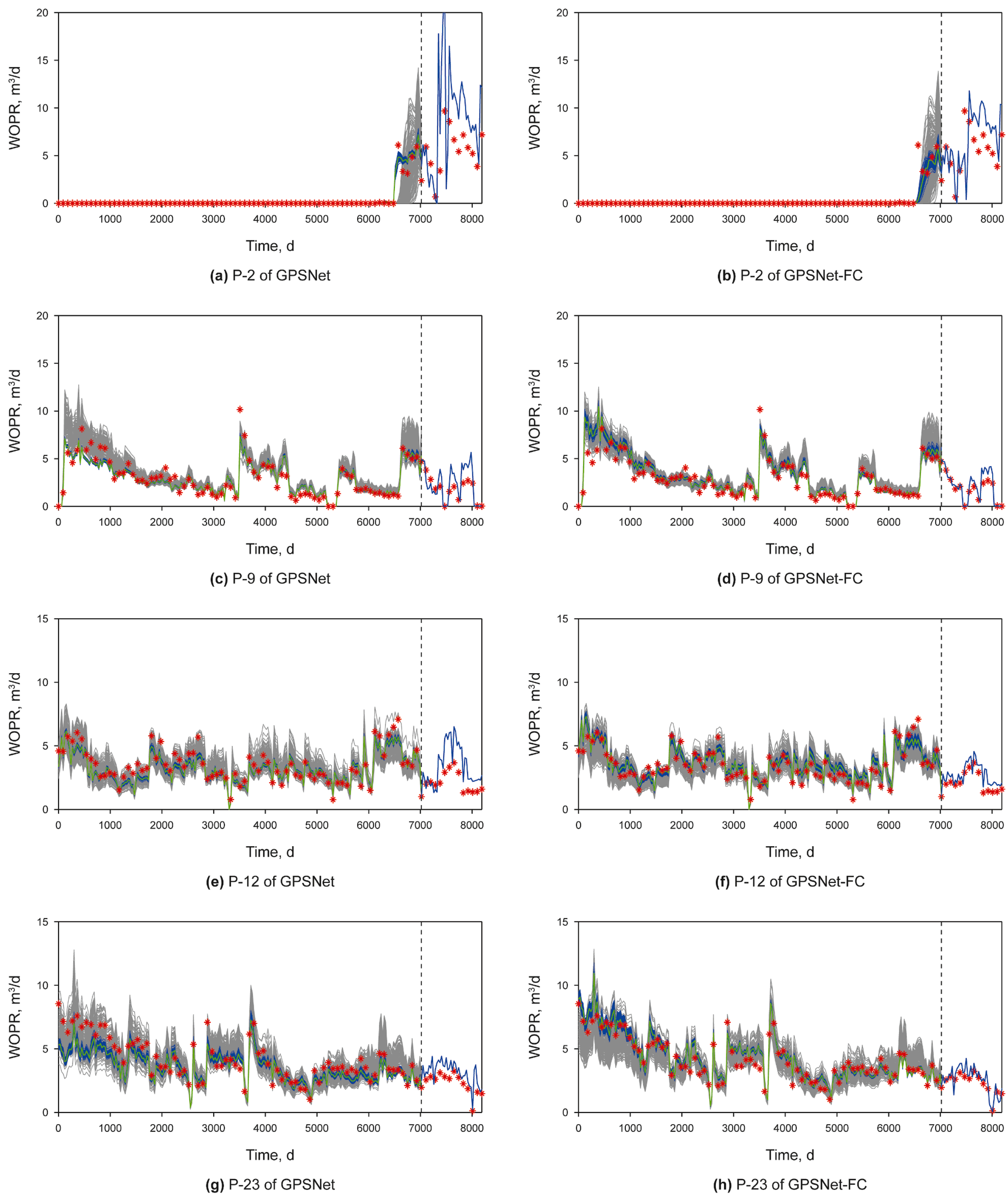

Fig. 30. History-matching and prediction performance of several production wells in Example 4 using the GPSNet and GPSNet-FC models. **(a)** P-2 of GPSNet. **(b)** P-2 of GPSNet-FC. **(c)** P-9 of GPSNet. **(d)** P-9 of GPSNet-FC. **(e)** P-12 of GPSNet. **(f)** P-12 of GPSNet-FC. **(g)** P-23 of GPSNet. **(h)** P-23 of GPSNet-FC. The black dashed vertical line separates the history-matching and prediction stages. In the history-matching stage, the gray curves represent the prior ensemble, the blue curves represent the posterior ensemble, the green curve denotes the posterior mean, and the red dots indicate the observed data. In the prediction stage, the blue line shows the model prediction results, while the red dots represent the observed values. After 15 history-matching assimilation steps, the posterior ensemble had already converged strongly, causing the mean curve to almost completely overlap with the posterior ensemble. As a result, the blue posterior curves are not clearly visible in the figure.

significantly expanded, allowing wells to be fully shut in (rate = 0) when necessary. The green curve in Fig. 26 shows the optimization result obtained under this enlarged search space. It can be observed that the water cut did not decrease significantly compared to the red curve; therefore, the improvement in FOPT is primarily driven by the enhancement of injection and production rates. This demonstrates that a broader rate domain allows the optimizer to explore more aggressive well-control strategies and identify theoretical solutions with superior production performance. These results confirm that the GPSNet-FC model remains robust and computationally efficient even when the feasible range is extended to include zero-rate conditions.

Table 6 presents a detailed comparison of the prediction and optimization results shown in Fig. 26. The findings indicate a significant increase in oil production following polymer injection. Compared with Cartesian grid, the optimal injection and production strategies determined by the GPSNet-FC model have similar recovery rates and water cuts during displacement, but the GPSNet-FC model achieves optimization in only one-fifth of the time required by Cartesian grid, highlighting its capability to enhance optimization efficiency. These results confirm that the GPSNet-FC model provides a fast and reliable technical framework for oilfield decision-making.

To assess the relative importance of varying water cost versus polymer cost, we conducted a comparative test with two different cost settings: Low water cost scenario: water injection cost of 6.18 USD/m^3 and water production cost of 4.63 USD/m^3, polymer cost of 2527.2 USD/t. High water cost scenario: water injection cost of 10 USD/m^3 and water production cost of 15 USD/m^3 (based on (Dai et al., 2026)).

The optimization results of injection rate and polymer concentration under low and high water cost scenarios are shown in Fig. 27. It can be observed that when the water cost is relatively low, the optimization tends to select a lower polymer concentration and a higher injection rate to improve sweep efficiency. In contrast, when the water cost is high, the optimization favors a relatively higher polymer concentration with a lower injection rate, indicating that the cost of water significantly influences the optimization trend. The detailed economic cost and the corresponding NPV values are presented in Fig. 27(e). Although the total injected water volume decreases under the high water cost scenario, the overall costs associated with water injection and production increase substantially, while the polymer-related costs are nearly the same under both scenarios. Consequently, the NPV declines markedly as the water cost increases, suggesting that the optimization shifts toward a more cost-effective operational strategy that minimizes water-handling expenses.

3.4. Example 4: application to an actual oil field block

In order to verify the practical application of the GPSNet-FC model, we applied it to an actual field X. This field has four types of sedimentary facies distribution which were identified and shown in Fig. 28(a). The colors blue, green, yellow, and red represent four sedimentary facies, with permeability ranges of 0–2000, 2000–4000, 4000–6000, and 6000–8000 mD, respectively. Sedimentary facies boundaries are depicted by bright yellow curves. This example was modeled using a two-dimensional flow network because the reservoir exhibits limited vertical heterogeneity and is dominated by lateral flow behavior. The average pay thickness is approximately 10–15 m, and both injection and production wells are completed over the same interval without zonal isolation. Consequently, vertical permeability contrasts and cross-layer flow are negligible, and a 2D representation adequately captures the dominant areal sweep pattern. This simplification allows for efficient history matching and production optimization without sacrificing accuracy, which aligns with the intended application of GPSNet-FC as a rapid, physics-based decision-support tool. The average porosity of the field is 0.23, and the specific reservoir parameters are listed in Table 7. The oil field has been in operation since the late 1990s, with a total of 57 wells, including 10 injection wells and 47 production wells. After years of waterflood development, the field's water cut has exceeded 90%. The subsequent development plan for injecting polymer solution needs to be optimized for reducing the water cut. At the same time, to demonstrate the effect of integrating depositional facies modeling within the GPSNet-FC framework, we

Table 8
History matching and prediction errors of several production wells for the GPSNet and GPSNet-FC models in Example 4.

Error, %	P-5	P-5	P-5	P-5	FOPT	FWCT
GPSNet-HM	14.91	19.52	21.46	30.84	0.01	0.23
GPSNet-FC -HM	8.91	19.69	18.01	12.77	0.01	0.20
GPSNet-prediction	454.28	59.20	505.27	75.41	13.78	133.16
GPSNet-FC-prediction	241.10	53.95	55.69	36.03	0.7	13.69

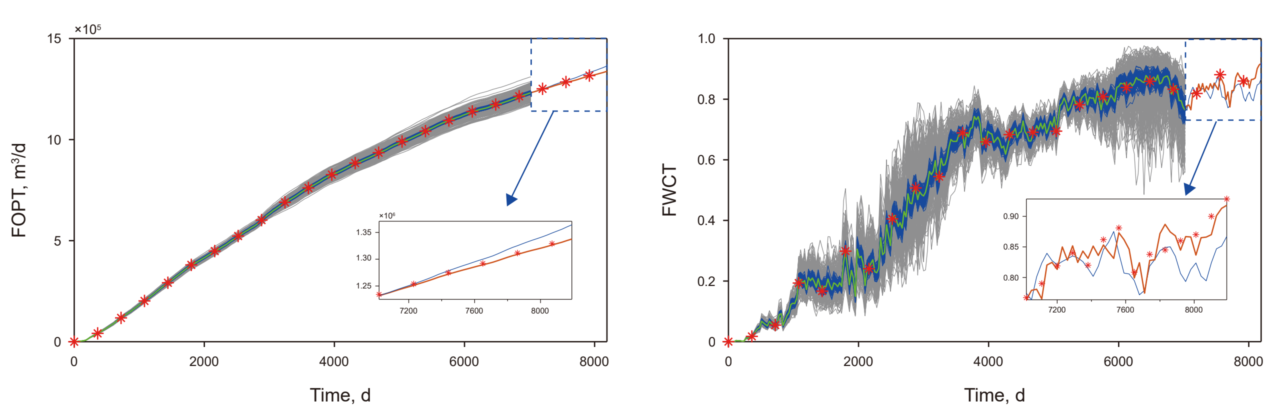

(a) History matching and prediction of FOPT **(b)** History matching and prediction of FWCT

Fig. 31. History-matching and prediction performance of the field in Example 4 using the GPSNet and GPSNet-FC models. (**a**) History matching and prediction of FOPT. (**b**) History matching and prediction of FWCT. For comparison, the results of both GPSNet and GPSNet-FC are presented together. In the history-matching stage, the results shown correspond to the GPSNet-FC model, where the gray curves represent the prior ensemble, the blue curves represent the posterior ensemble, the green curve denotes the posterior mean, and the red dots indicate the observed data. In the prediction stage, the blue curve represents the GPSNet results, while the orange curve represents the GPSNet-FC results.

also constructed a GPSNet model for comparison. The difference between the two models lies not in the fitting accuracy during history matching, but in the prediction accuracy after history matching. History matching is inherently non-unique, as different parameter combinations may yield similar fitting results. However, parameter sets that deviate from the actual geological conditions

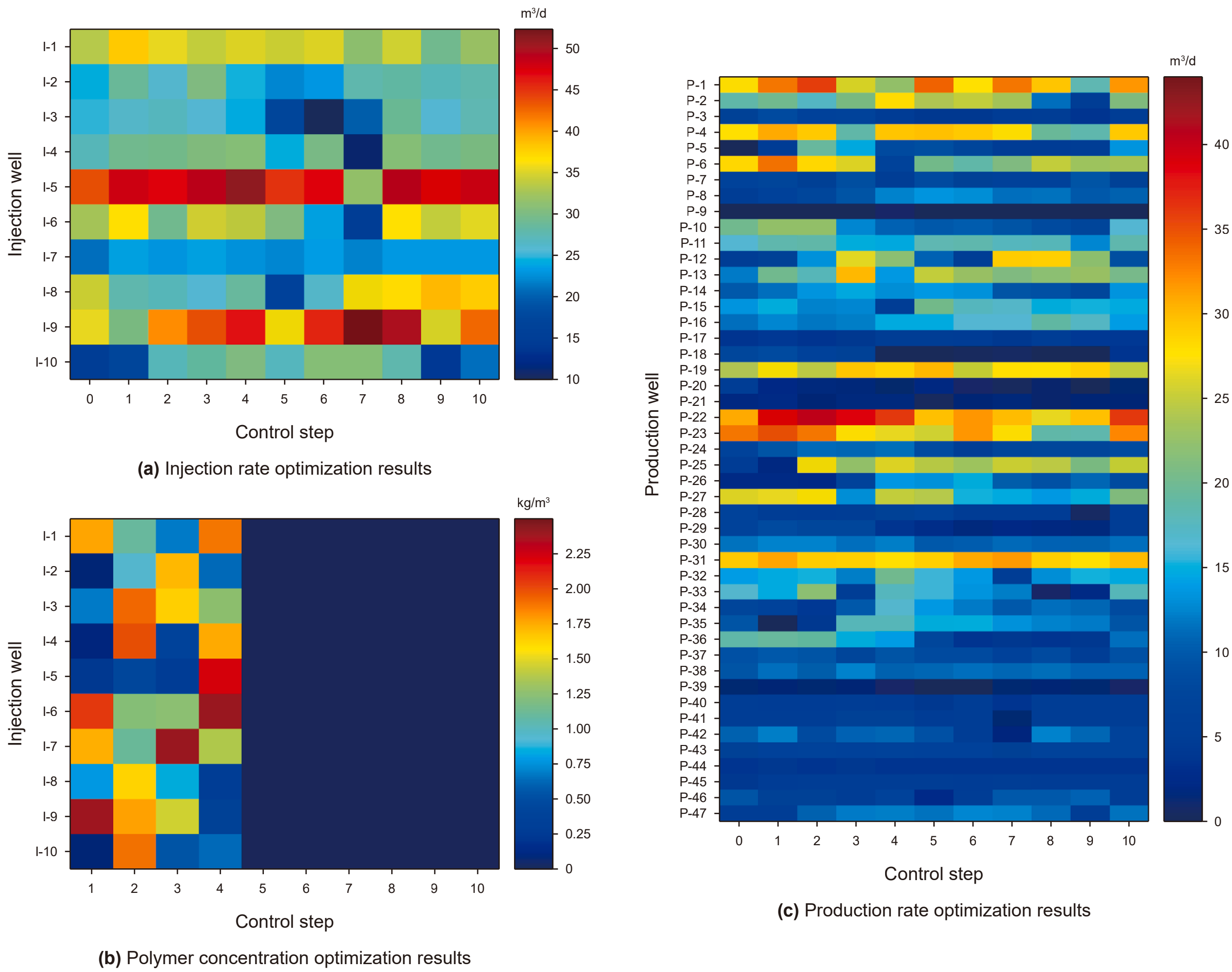

Fig. 32. Well production optimization results in Example 4. **(a)** Injection rate optimization results. **(b)** Polymer concentration optimization results. **(c)** Production rate optimization results. The vertical axis represents the optimized wells, and the horizontal axis represents the optimized time steps. Each colored block shows the magnitude of the optimization result, with red indicating larger values and blue indicating smaller values.

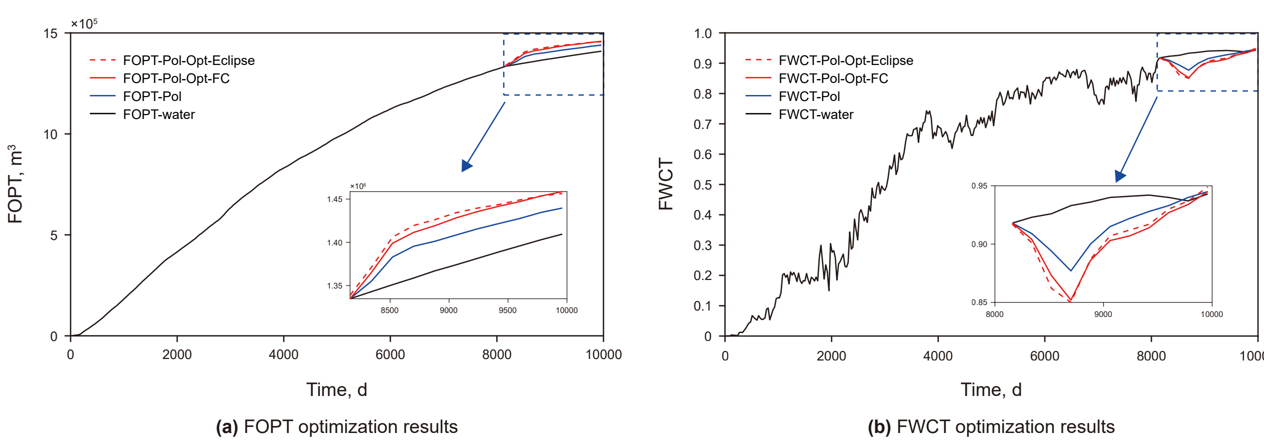

Fig. 33. Field production optimization results. **(a)** FOPT optimization results. **(b)** FWCT optimization results. The black curve represents the water flooding prediction, the blue curve represents the polymer flooding prediction, the blue curve represents the predicted results with a constant total polymer injection, uniformly injected, and the red dashed curve illustrates the performance of this optimized schedule when implemented in the full-grid Eclipse model.

often lead to poor predictive performance. By embedding sedimentary facies constraints in both the prior model generation and the history-matching process, we effectively reduce the non-uniqueness of the history-matching solutions and improve the predictive reliability of the model.

Therefore, we first used the initial 7020 days of production history (out of a total of 8190 days) for history matching and compared the prediction performance of the two models over the remaining 1170 days. Subsequently, the entire 8190-day production history was used for history matching and subsequent production optimization. The optimized results were then compared with the field strategy of constant total polymer injection uniformly injected to verify the effectiveness of the proposed model.

Firstly, the GPSNet and GPSNet-FC models were constructed based on the actual well locations and perforation information from the field. The well pattern and the initial permeability fields of the two models are presented in Fig. 29(a) and (b). In these figures, the initial permeability fields are overlaid on the depositional facies map to provide a clearer visualization of the permeability distribution. In the GPSNet model, uniform permeability values were assigned within each connection, whereas in the GPSNet-FC model, permeability was assigned according to the depositional facies distribution, consistent with Example 2. Both models were then calibrated through history matching using the oil production rate as the observation data, and four production wells were selected for illustration. The prior permeability (in ln) of each facies was sampled within ± 0.4 mD around its initial permeability, and the prior grid volumes were sampled within the range of [0.5, 2] times their initial values. The single-well and field-scale fitting and prediction results of the two models are shown in Figs. 30 and 31, while the corresponding history-matching and prediction errors are summarized in Table 8. In the figure, the gray dashed line divides the time axis into the history-matching and prediction stages. During the history-matching stage, the prior ensemble is shown as gray curves, the posterior ensemble as blue curves, the posterior mean as the green curve, and the actual field observations as the red dots. In the prediction stage, the blue curve represents the prediction from the optimal history-matched model, while the red dots denote the measured field data. As shown in Figs. 29 and 30 and Table 8, due to the strong data-assimilation capability of the ESMDA algorithm, both models achieve satisfactory fitting performance during the history-matching stage. However, in the prediction stage, the GPSNet-FC model exhibits more reliable and stable forecasting behavior. The optimal posterior permeability fields obtained from the two models are displayed in Fig. 29(c) and (d). Compared with GPSNet, the permeability field estimated by GPSNet-FC shows stronger consistency with the depositional facies distribution.

After re-matching the entire historical period (8190 days) using the GPSNet-FC model, polymer flooding production optimization was subsequently performed, and the history-matching process is not shown here. In this optimization process, each time step corresponds to 180 days, and the optimization was performed 10 steps, totaling 5 years. The first 4 steps were focused on polymer injection, while the remaining 6 steps were allocated to water injection. The optimized production schedule is shown in Fig. 32.

The GPSNet-FC model is designed to replace the construction of complex full-physics reservoir models. In this example, to evaluate the optimization performance on a full-grid simulation, a corresponding full-grid Eclipse model was also constructed, as shown in Fig. 28(b). Fig. 33 presents the results of water flooding prediction, polymer flooding with constant total polymer injection (uniformly injected), and polymer flooding optimization using the GPSNet-FC model. Similar to Example 3, the black curve represents the predicted results obtained by maintaining the last time step's injection-production scheme from the history matching stage. The blue curve represents the predicted results with a constant total polymer injection, uniformly injected. The red curve represents the optimized results for polymer flooding. Compared to the blue curve, the red curve shows an 18.12% increase in cumulative oil production. These results confirm that the GPSNet-FC model, incorporating sedimentary facies, is capable of enhancing production optimization in real-world oil field applications.

4. Conclusion

This study proposes a facies-constrained flow-network model (GPSNet-FC) to address the computational inefficiency of high-fidelity simulations and the geological inconsistency of traditional flow-network models in the CLRM of polymer flooding reservoirs. The main contributions of this study are as follows: (1) The developed methodology synergistically combines edge detection techniques with level set functions to establish a novel framework for sedimentary facies characterization. By integrating facies-specific petrophysical properties during model initialization and enforcing geological consistency through facies-constrained history matching, the proposed GPSNet-FC demonstrates significant improvements over conventional approaches. This geological regularization strategy effectively mitigates solution non-uniqueness while maintaining computational efficiency, achieving enhanced predictive performance without compromising history matching accuracy. (2) It establishes the application of flow-network models for polymer flooding optimization through two key advancements: development of a dimension-reduced modeling framework that preserves essential geological features through facies-constrained parameterization; successful implementation of a closed-loop optimization workflow that synergizes geological constraints with production dynamics. Field-scale validation confirms the model's capability to deliver economically optimized polymer injection strategies with measurable improvements in both oil recovery and water cut management.

As the first integration of sedimentary facies constraints in flow-network modeling and the inaugural GPSNet adaptation for polymer flooding optimization, this study establishes a new paradigm for bridging geological characterization with rapid reservoir management. The GPSNet-FC framework advances simplified model development by maintaining geological fidelity while enabling real-time decision-making capabilities, particularly for complex enhanced oil recovery processes.

The current GPSNet-FC framework is implemented within a 2D facies-constrained flow network that effectively captures lateral heterogeneity and connectivity, but it does not explicitly model vertical layering, inter-layer cross-flow, or depth-dependent (vertical) variations in permeability, adsorption or sweep efficiency. In applications where vertical flow or gravity/thermal segregation is negligible (thin formations, dominantly lateral flow), this 2D simplification is justified and enables rapid history-matching and optimization. However, in reservoirs with significant vertical heterogeneity, layering or gravity/thermal effects—such as those encountered in thick steamflood formations-the model fidelity may be compromised. Drawing from the workflow applied by (Wang et al., 2022) in a steamflood sector model, which mapped the flow network into 2-D *x*-*z* vertical slices to capture vertical flow paths, we propose a layered or quasi-3D extension of GPSNet-FC in future work whereby multiple horizontally-distributed flow networks are stacked and coupled via interlayer transmissibility. This enhanced version would capture vertical sweep, layer interconnectivity and vertical propagation of polymer/thermal fronts while retaining the computational efficiency advantages of a network surrogate. The proposed GPSNet-FC workflow is inherently extendable to three-dimensional (3D) flow networks, and only minimal modifications are required to adapt the methodology to 3D cases. The core structure of the workflow-comprising (1) network construction, (2) facies identification and parameterization, (3) data assimilation (history matching), and (4) production optimization-remains unchanged. The key difference lies in how geometric mapping, facies assignment, and inter-layer connectivity are handled in a 3D framework.

Specifically, when impermeable interlayers exist in the reservoir, the modeling process can be extended to a multi-layer 3D structure, where each layer is independently characterized by its own sedimentary facies distribution and petrophysical parameters. The inter-layer relationships are represented by vertical connections through well grid cells, while lateral communication between different layers is restricted, resulting in a layered 3D flow-network model. Conversely, in the absence of interlayers, vertical communication between layers can be established, allowing inter-layer transmissibility to be considered during the network construction. This flexibility ensures that the proposed workflow can effectively represent both stratified and fully communicating 3D reservoirs, maintaining geological realism while preserving computational efficiency.

In addition, with respect to surrogate and hybrid modelling approaches in reservoir management, models such as the Capacitance Resistance Model (CRM) and INSIM offer very fast runtimes but sacrifice geological fidelity and are often limited to waterflood or linear flow regimes. In comparison, GPSNet-FC combines the computational advantage of reduced-order modelling with richer geological structure (via facies constraints) and supports nonlinear EOR processes (e.g., polymer flooding). Therefore, it occupies a middle ground: more physically realistic and geologically informed than CRM/INSIM, yet far less computationally demanding than full 3D geocellular simulation.

CRediT authorship contribution statement

Guo-Yu Qin: Writing – original draft, Visualization, Validation, Software, Methodology, Investigation, Data curation. **Xia Yan:** Writing – review & editing, Validation, Supervision, Project administration, Methodology, Investigation, Funding acquisition, Formal analysis, Conceptualization. **Kai Zhang:** Writing – review & editing, Supervision, Resources, Funding acquisition, Conceptualization. **Li-Ming Zhang:** Writing – review & editing, Investigation, Funding acquisition. **Qi Zhang:** Writing – review & editing, Investigation, Formal analysis. **Ming-Xin Zhang:** Writing – original draft, Software, Methodology, Investigation. **Chen-Yang Wang:** Software, Data curation.

Declaration of competing interest

The authors declare that they have no known competing financial interests or personal relationships that could have appeared to influence the work reported in this paper.

Acknowledgments

This work was supported by the National Natural Science Foundation of China (Nos. 52474067, 52441411, 52325402, 52034010, and 12131014), Natural Science Foundation of Shandong Province, China (No. ZR2024ME005), Fundamental Research Funds for the Central Universities (Nos. 25CX02025A and 21CX06031A), Youth Innovation and Technology Support Program for Higher Education Institutions of Shandong Province, China (No. 2022KJ070).

References

Arps, J.J., 1945. Analysis of decline curves. Transac. AIME 160 (1), 228–247. https://doi.org/10.2118/945228-G.
Bai, W.-P., Cheng, S.-Q., Guo, X.-Y., Wang, Y., Guo, Q., Tan, C.-D., 2024. Oilfield analogy and productivity prediction based on machine learning: Field cases in PL oilfield, China. Pet. Sci. 21 (4), 2554–2570. https://doi.org/10.1016/j.petsci.2024.02.018.
Brooks, R.H., 1965. Hydraulic Properties of Porous Media. Colorado State University.
Cai, J., Qin, X., Xia, X., Jiao, X., Chen, H., Wang, H., Xia, Y., 2024. Numerical modeling of multiphase flow in porous media considering micro-and nanoscale effects: A comprehensive review. Gas Sci. Eng. 131, 205441. https://doi.org/10.1016/j.jgsce.2024.205441.
Cao, F., Luo, H., Lake, L.W., 2014. Development of a fully coupled two-phase flow based capacitance resistance model CRM. In: SPE Improved Oil Recovery Symposium, SPE-169485-MS. https://doi.org/10.2118/169485-MS.
Dai, Q., Zhang, L., Zhang, K., Chen, G., Chen, Z., Xue, X., Wang, Y., Wang, Z., Di, C., Zhao, F., 2026. Carbon-pricing optimization framework for oilfield carbon dioxide-water alternation with economic and environmental gains. Energy Convers. Manag. 348, 120613. https://doi.org/10.1016/j.enconman.2025.120613.
Das, S., Suganthan, P.N., 2010. Differential evolution: A survey of the state-of-the-art. IEEE Trans. Evol. Comput. 15 (1), 4–31. https://doi.org/10.1109/TEVC.2010.2059031.
Datta-Gupta, A., King, M.J., 2007. Streamline Simulation: Theory and practice. Society of Petroleum Engineers Richardson.
Dong, Z., Pan, X., Li, W., Wei, X., Qian, S., Hou, B., Zou, L., Lin, K., Yi, H., 2024. Using polymer-alternating-water to maximize polymer flooding performance. J. Pet. Explor. Prod. Technol. 14 (6), 1589–1604. https://doi.org/10.1007/s13202-024-01782-y.
Du, B., Zhang, F., Dontsov, E., Meng, K., 2025. Numerical simulation of hydraulic fracturing optimization in multi-well and multi-layer shale gas development: Insights from inter-well interference analysis. Geoenergy Sci. Eng. 250, 213825. https://doi.org/10.1016/j.geoen.2025.213825.
Durlofsky, L.J., 2005. Upscaling and gridding of fine scale geological models for flow simulation. In: 8th International Forum on Reservoir Simulation Iles Borromees, pp. 1–59.
Emerick, A.A., Reynolds, A.C., 2013. Ensemble smoother with multiple data assimilation. Comput. Geosci. 55, 3–15. https://doi.org/10.1016/j.cageo.2012.03.011.
Evensen, G., 1994. Sequential data assimilation with a nonlinear quasi-geostrophic model using Monte Carlo methods to forecast error statistics. J. Geophys. Res. Oceans 99 (C5), 10143–10162. https://doi.org/10.1029/94JC00572.
Evensen, G., 2018. Analysis of iterative ensemble smoothers for solving inverse problems. Comput. Geosci. 22 (3), 885–908. https://doi.org/10.1007/s10596-018-9731-y.
Fang, J., Wang, X., Ji, B., Zou, P., Cheng, S., Dai, C., 2024. Microscopic behavior of heteroatom asphaltene in the multi-media model: The effect on heavy oil properties. Geoenergy Sci. Eng. 241, 213180. https://doi.org/10.1016/j.geoen.2024.213180.
Grave, M., da Silva Castro, E., Pesco, S., Junior, A.B.B., da Silva Gasparini, L., Cavalcante, R.G., da Costa Alves, R.R., Rodrigues, J.R.P., 2024. A mass conservative INSIM-FT-3D physics-based data-driven oil-water reservoir simulator. Geoenergy Sci. Eng. 241, 213102. https://doi.org/10.1016/j.geoen.2024.213102.
Griffiths, I.B., 1998. The Extreme Spearman Rank Correlation Coefficient in the Characterization of the North Buck Draw Field. University of Texas at Austin.
Guan, X., Wang, Z., Ren, G., Hui, M., Kazanov, D., Wen, X.-H., 2024. Fast history matching with a customized physics-based data-driven flow network model GPSNet: Application to a giant deep-water gas field. In: SPE Annual Technical Conference and Exhibition. https://doi.org/10.2118/220856-MS.
Guo, Z., Reynolds, A.C., 2019. INSIM-FT in three-dimensions with gravity. J. Comput. Phys. 380, 143–169. https://doi.org/10.1016/j.jcp.2018.12.016.
Guo, Z., Reynolds, A.C., Zhao, H., 2017. A Physics-based data-driven Model for history-matching, prediction and characterization of waterflooding performance. In: SPE Reservoir Simulation Conference. https://doi.org/10.2118/182660-MS.
Guo, Z., Reynolds, A.C., Zhao, H., 2018. Waterflooding optimization with the INSIM-FT data-driven model. Comput. Geosci. 22, 745–761. https://doi.org/10.1007/s10596-018-9723-y.
He, H., Chen, R., Yuan, F., Tian, Y., Ning, W., 2024. Influence of viscosity ratio on enhanced oil recovery performance of anti-hydrolyzed polymer for high-temperature and high-salinity reservoir. Phys. Fluids 36 (4). https://doi.org/10.1063/5.0203304.
He, J., 2013. Reduced-order modeling for oil-water and compositional systems, with application to data assimilation and production optimization. Stanford University, 28122419.
Hoffmann, A., Stanko, M., González, D., 2019. Optimized production profile using a coupled reservoir-network model. J. Pet. Explor. Prod. Technol. 9 (3), 2123–2137. https://doi.org/10.1007/s13202-019-0613-1.

Hou, J., Zhou, K., Zhang, X.-S., Kang, X.-D., Xie, H., 2015. A review of closed-loop reservoir management. Pet. Sci. 12, 114–128. https://doi.org/10.1007/s12182-014-0005-6.
Jacquard, P., 1965. Permeability distribution from field pressure data. Soc. Petrol. Eng. J. 5 (4), 281–294. https://doi.org/10.2118/1307-PA.
Jähne, B., 2005. Digital Image Processing. Springer.
Jansen, J.-D., Douma, S., Brouwer, D.R., Van den Hof, P., Bosgra, O., Heemink, A., 2009. Closed-Loop Reservoir Management. In: SPE Reservoir Simulation Symposium, SPE-119098-MS. https://doi.org/10.2118/119098-MS.
Jo, H., Jung, H., Ahn, J., Lee, K., Choe, J., 2017. History matching of channel reservoirs using ensemble Kalman filter with continuous update of channel information. Energy Explor. Exploit. 35 (1), 3–23. https://doi.org/10.1177/0144598716680141.
Jung, H., Jo, H., Kim, S., Lee, K., Choe, J., 2017. Recursive update of channel information for reliable history matching of channel reservoirs using EnKF with DCT. J. Petrol. Sci. Eng. 154, 19–37. https://doi.org/10.1016/j.petrol.2017.04.016.
Kadeethum, T., Ballarin, F., Choi, Y., O'Malley, D., Yoon, H., Bouklas, N., 2022. Non-intrusive reduced order modeling of natural convection in porous media using convolutional autoencoders: Comparison with linear subspace techniques. Adv. Water Resour. 160, 104098. https://doi.org/10.1016/j.advwatres.2021.104098.
Kiærr, A., Lødøen, O., De Bruin, W., Barros, E., Leeuwenburgh, O., 2020. Evaluation of a data-driven flow network model (Flownet) for reservoir prediction and optimization. European Association of Geoscientists & Engineers, pp. 1–18. https://doi.org/10.3997/2214-4609.202035099.
King, M., MacDonald, D., Todd, S., Leung, H., 1998. Application of novel upscaling approaches to the Magnus and Andrew Reservoirs. In: SPE Europec Featured at EAGE Conference and Exhibition, SPE-50643-MS. https://doi.org/10.2118/50643-MS.
Leeuwenburgh, O., Egberts, P.J., Barros, E.G., Turchan, L.P., Dilib, F., Lødøen, O.-P., de Bruin, W.J., 2024. A hybrid data-physics framework for reservoir performance prediction with application to H_2S production. SPE J. 29 (2), 1161–1177. https://doi.org/10.2118/218000-PA.
Lerlertpakdee, P., Jafarpour, B., Gildin, E., 2014. Efficient production optimization with flow-network models. SPE J. 19 (6), 1083–1095. https://doi.org/10.2118/170241-PA.
Li, C., King, M.J., 2020. Integration of pressure transient data into reservoir models using the fast marching method. SPE J. 25 (4), 1557–1577. https://doi.org/10.2118/180148-PA.
Li, C., Wang, Z., King, M.J., 2021. Transient drainage volume characterization and flow simulation in reservoir models using the fast marching method. Comput. Geosci. 25 (5), 1647–1666. https://doi.org/10.1007/s10596-021-10061-2.
Li, Y., Alpak, F.O., Jain, V., Lu, R., Onur, M., 2023. History-matching and forecasting production rate and bottomhole pressure data using an enhanced physics-based data-driven simulator. SPE Reserv. Eval. Eng. 26 (3), 957–974. https://doi.org/10.2118/210102-PA.
Li, Y., Onur, M., 2023. INSIM-BHP: A physics-based data-driven reservoir model for history matching and forecasting with bottomhole pressure and production rate data under waterflooding. J. Comput. Phys. 473, 111714. https://doi.org/10.1016/j.jcp.2022.111714.
Lin, J.-Q., Yan, X., Wang, E.-Z., Zhang, Q., Zhang, K., Liu, P.-Y., Zhang, L.-M., 2025. A layer-specific constraint-based enriched physics-informed neural network for solving two-phase flow problems in heterogeneous porous media. Pet. Sci. 22 (11), 4714–4735. https://doi.org/10.1016/j.petsci.2025.07.008.
Lutidze, G., 2018. StellNet: Physics-based data-driven general model for closed-loop reservoir management. The University of Tulsa, 10976002.
Nasir, Y., Durlofsky, L.J., 2024. Multi-asset closed-loop reservoir management using deep reinforcement learning. Comput. Geosci. 28 (1), 23–42. https://doi.org/10.1007/s10596-023-10255-w.
Naudomsup, N., Lake, L.W., 2019. Extension of capacitance/resistance model to tracer flow for determining reservoir properties. SPE Reserv. Eval. Eng. 22 (1), 266–281. https://doi.org/10.2118/187410-PA.
Osher, S., Fedkiw, R., Piechor, K., 2004. Level set methods and dynamic implicit surfaces. Appl. Mech. Rev. 57 (3), B15. https://doi.org/10.1115/1.1760521. -B15.
Osher, S., Fedkiw, R.P., 2001. Level set methods: an overview and some recent results. J. Comput. Phys. 169 (2), 463–502. https://doi.org/10.1006/jcph.2000.6636.
Pan, Y., Deng, L., Zhou, P., Lee, W.J., 2021. Laplacian echo-state networks for production analysis and forecasting in unconventional reservoirs. J. Petrol. Sci. Eng. 207, 109068. https://doi.org/10.1016/j.petrol.2021.109068.
Paredes, J., Perez, R., Larez, C., 2013. Evolution strategy algorithm through assisted history matching and well placement optimization to enhance ultimate recovery factor of naturally fractured reservoirs. In: SPE Reservoir Characterisation and Simulation Conference and Exhibition, SPE-165943-MS. https://doi.org/10.2118/165943-MS.
Parekh, B., Kabir, C.S., 2013. A case study of improved understanding of reservoir connectivity in an evolving waterflood with surveillance data. J. Petrol. Sci. Eng. 102, 1–9. https://doi.org/10.1016/j.petrol.2013.01.004.
Rao, X., He, X., Kwak, H., Yousef, A., Hoteit, H., 2024. A novel streamline simulation method for fractured reservoirs with full-tensor permeability. Phys. Fluids 36 (1). https://doi.org/10.1063/5.0176665.
Rao, X., Xu, Y., Liu, D., Liu, Y., Hu, Y., 2021. A general physics-based data-driven framework for numerical simulation and history matching of reservoirs. Adv. Geo-Energy Res. 5 (4). https://doi.org/10.46690/ager.2021.04.07.
Remy, N., 2009. Applied Geostatistics with Sgems: a User's Guide. Cambridge University Press.
Ren, G., He, J., Wang, Z., Younis, R.M., Wen, X.-H., 2019. Implementation of physics-based data-driven models with a commercial simulator. In: SPE Reservoir Simulation Conference, SPE-193855-MS. https://doi.org/10.2118/193855-MS.
Ren, G., Wang, Z., Lin, Y., Onishi, T., Guan, X., Wen, X.-H., 2023. A fast history matching and optimization tool and its application to a full field with more than 1,000 Wells. SPE J. 29 (10), 5538–5558.. https://doi.org/10.2118/212188-PA.
Salem, K.G., Salem, A.M., Tantawy, M.A., Gawish, A.A., Gomaa, S., El-hoshoudy, A., 2024a. A comprehensive investigation of nanocomposite polymer flooding at reservoir conditions: New insights into enhanced oil recovery. J. Polym. Environ. 32 (11), 5915–5935. https://doi.org/10.1007/s10924-024-03336-z.
Salem, K.G., Tantawy, M.A., Gawish, A.A., Salem, A.M., Gomaa, S., El-hoshoudy, A., 2024b. Key aspects of polymeric nanofluids as a new enhanced oil recovery approach: A comprehensive review. Fuel 368, 131515. https://doi.org/10.1016/j.fuel.2024.131515.
Shen, Y., Wu, J., Ma, M., Du, X., Wu, H., Fei, X., Niu, D., 2024. Improved differential evolution algorithm based on cooperative multi-population. Eng. Appl. Artif. Intell. 133, 108149. https://doi.org/10.1016/j.engappai.2024.108149.
Tadjer, A., Hong, A., Bratvold, R., 2022. Bayesian deep decline curve analysis: A new approach for well oil production modeling and forecasting. SPE Reserv. Eval. Eng. 25 (3), 568–582. https://doi.org/10.2118/209616-PA.
Tariq, Z., Mahmoud, M., Al-Shehri, D., Sibaweihi, N., Sadeed, A., Hossain, M.E., 2018. A stochastic optimization approach for profit maximization using alkaline-surfactant-polymer flooding in complex reservoirs. In: SPE Kingdom of Saudi Arabia Annual Technical Symposium and Exhibition, SPE-192243-MS. https://doi.org/10.2118/192243-MS.
Tchelepi, H.A., Jenny, P., Lee, S.H., Wolfsteiner, C., 2007. Adaptive multiscale finite-volume framework for reservoir simulation. SPE J. 12 (2), 188–195. https://doi.org/10.2118/93395-PA.
Tellez Arellano, A.G., Hassan, A.M., Al-Shalabi, E.W., AlAmeri, W., Kamal, M.S., Patil, S., 2023. An extensive evaluation of different reservoir simulators used for polymer flooding modeling. In: SPE Gas & Oil Technology Showcase and Conference, SPE-214088-MS. https://doi.org/10.2118/214088-MS.
Torre, V., Poggio, T.A., 1986. On edge detection. IEEE Trans. Pattern Anal. Mach. Intell. (2), 147–163. https://doi.org/10.1109/TPAMI.1986.4767769.
Tostado, M., Popa, A.S., Cassidy, S., Shepeherd, D., 2016. An analytical approach for well production history matching in a heavy oil reservoir. In: SPE Western Regional Meeting, SPE-180371-MS. https://doi.org/10.2118/180371-MS.
Valkó, P.P., 2009. Assigning value to stimulation in the Barnett Shale: A simultaneous analysis of 7000 plus production hystories and well completion records. In: SPE Hydraulic Fracturing Technology Conference and Exhibition, SPE-119369-MS. https://doi.org/10.2118/119369-MS.
Wang, D., Seright, R.S., Shao, Z., Wang, J., 2008. Key aspects of project design for polymer flooding at the Daqing Oilfield. SPE Reserv. Eval. Eng. 11 (6), 1117–1124. https://doi.org/10.2118/109682-PA.
Wang, J.-L., Zhang, L.-M., Zhang, K., Wang, J., Zhou, J.-P., Peng, W.-F., Yin, F.-L., Zhong, C., Yan, X., Liu, P.-Y., 2024. Multi-surrogate framework with an adaptive selection mechanism for production optimization. Pet. Sci. 21 (1), 366–383. https://doi.org/10.1016/j.petsci.2023.08.028.
Wang, S., Sobecki, N., Ding, D., Zhu, L., Wu, Y.-S., 2019. Accelerating and stabilizing the vapor-liquid equilibrium (VLE) calculation in compositional simulation of unconventional reservoirs using deep learning based flash calculation. Fuel 253, 209–219. https://doi.org/10.1016/j.fuel.2019.05.023.
Wang, Y., Yang, S.-L., Xie, H., Jiang, Y., Cheng, S.-Q., Zhang, J., 2025. Dynamic characterization of viscoelasticity during polymer flooding: a two-phase numerical well test model and field study. Pet. Sci. 22 (6), 2493–2501. https://doi.org/10.1016/j.petsci.2025.04.029.
Wang, Z., Guan, X., Milliken, W., Wen, X.-H., 2022. Fast history matching and robust optimization using a novel physics-based data-driven flow network model: An application to a steamflood sector model. SPE J. 27 (4), 2033–2051. https://doi.org/10.2118/209611-PA.
Wang, Z., He, J., Milliken, W.J., Wen, X.-H., 2021. Fast history matching and optimization using a novel physics-based data-driven model: an application to a diatomite reservoir. SPE J. 26 (6), 4089–4108. https://doi.org/10.2118/200772-PA.
Wen, X.-H., Gómez-Hernández, J.J., 1996. Upscaling hydraulic conductivities in heterogeneous media: An overview. J. Hydrol. 183 (1–2). https://doi.org/10.1016/S0022-1694(96)80030-8 ix-xxxii.
Xu, L., Zhao, H., Li, Y., Cao, L., Xie, X., Zhang, X., Li, Y., 2018. Production optimization of polymer flooding using improved Monte Carlo gradient approximation algorithm with constraints. J. Circ. Syst. Comput. 27 (11), 1850167. https://doi.org/10.1142/S0218126618501670.
Yan, K., Han, P., Xie, K., Meng, L., Cao, W., Cao, R., Zhang, T., Li, X., Li, S., 2024a. Identification and characterization of dominant seepage channels in oil reservoirs after polymer flooding based on streamline numerical simulation. Alex. Eng. J. 106, 704–720. https://doi.org/10.1016/j.aej.2024.08.104.
Yan, X., Lin, J., Ju, Y., Zhang, Q., Zhang, Z., Zhang, L., Yao, J., Zhang, K., 2025. A finite-volume based physics-informed fourier neural operator network for parametric learning of subsurface flow. Adv. Water Resour., 105087 https://doi.org/10.1016/j.advwatres.2025.105087.
Yan, X., Lin, J., Wang, S., Zhang, Z., Liu, P., Sun, S., Yao, J., Zhang, K., 2024b. Physics-informed neural network simulation of two-phase flow in heterogeneous and fractured porous media. Adv. Water Resour., 104731 https://doi.org/10.1016/j.advwatres.2024.104731.

Yan, X., Qin, G.-Y., Zhang, L.-M., Zhang, K., Yang, Y.-F., Yao, J., Wang, J.-L., Dai, Q.-Y., Wu, D.-W., 2024c. A dual-porosity flow-net model for simulating waterflooding in low-permeability fractured reservoirs. Geoenergy Sci. Eng. 240, 213069. https://doi.org/10.1016/j.geoen.2024.213069.
Yewgat, A., Busby, D., Chevalier, M., Lapeyre, C., Teste, O., 2022. Physics-constrained deep learning forecasting: An application with capacitance resistive model. Comput. Geosci. 26 (4), 1065–1100. https://doi.org/10.1007/s10596-022-10146-6.
Yousef, A.A., Gentil, P., Jensen, J.L., Lake, L.W., 2006. A capacitance model to infer interwell connectivity from production-and injection-rate fluctuations. SPE Reserv. Eval. Eng. 9 (6), 630–646. https://doi.org/10.2118/95322-PA.
Zalavadia, H., Sankaran, S., Kara, M., Sun, W., Gildin, E., 2019. A hybrid modeling approach to production control optimization using dynamic mode decomposition. In: SPE Annual Technical Conference and Exhibition, SPE-196124-MS. https://doi.org/10.2118/196124-MS.
Zhang, L., Wang, L., 2023. Optimization of site investigation program for reliability assessment of undrained slope using spearman rank correlation coefficient. Comput. Geotech. 155, 105208. https://doi.org/10.1016/j.compgeo.2022.105208.
Zhang, X., Ma, F., Yin, S., Wallace, C.D., Soltanian, M.R., Dai, Z., Ritzi, R.W., Ma, Z., Zhan, C., Lü, X., 2021. Application of upscaling methods for fluid flow and mass transport in multi-scale heterogeneous media: A critical review. Appl. Energy 303, 117603. https://doi.org/10.1016/j.apenergy.2021.117603.
Zhao, H., Kang, Z., Zhang, X., Sun, H., Cao, L., Reynolds, A.C., 2016. A physics-based data-driven numerical model for reservoir history matching and prediction with a field application. SPE J. 21 (6), 2175–2194. https://doi.org/10.2118/173213-PA.
Zhao, H., Liu, W., Rao, X., Sheng, G., Li, H.A., Guo, Z., Liu, D., Cao, L., 2021. INSIM-FPT-3D: A data-driven model for history matching, water-breakthrough prediction and well-connectivity characterization in three-dimensional reservoirs, SPE-203931-MS. https://doi.org/10.2118/203931-MS.
Zhao, H., Xu, L., Guo, Z., Zhang, Q., Liu, W., Kang, X., 2020. Flow-path tracking strategy in a data-driven interwell numerical simulation model for waterflooding history matching and performance prediction with infill wells. SPE J. 25 (2), 1007–1025. https://doi.org/10.2118/199361-PA.
Zhou, W., Fu, W., Liu, C., Zhang, K., Shen, J., Liu, P., Zhang, J., Zhang, L., Yan, X., 2024. Deep learning surrogate model-based randomized maximum likelihood for large-scale reservoir automatic history matching. Comput. Energy Sci. 1 (1), 17–27. https://compes.yandypress.com/index.php/3007-5602/article/view/9.